The Flare Irradiance Spectral Model - Version 2 (FISM2)

P. C. Chamberlin[1*], F. G. Eparvier[1], V. Knoer[1], H. Leise[1], A. Pankratz[1,2], M. Snow[1], B. Templeman[1], E. M. B. Thiemann[1], D. L. Woodraska[1], and T. N. Woods[1]

[1]Laboratory for Atmospheric and Space Physics, University of Colorado Boulder
[2]Rochester Institute of Technology, Rochester, NY

Key Points:

- FISM2 accurately models spectral irradiance variations due to the solar cycle, solar rotation, and solar flares.
- FISM2 fills temporal, from 1947-present, and spectral, from 0-190 nm, gaps in the measurements of SORCE/XPS, SDO/EVE, and SORCE/SOLSTICE.
- FISM2 is a much improved solar ultraviolet irradiance model over the first version released more than 15 years ago.

*3665 Discovery Drive, Boulder, CO 80303

Corresponding author: Phillip Chamberlin, Phil.Chamberlin@lasp.colorado.edu

Abstract

The Flare Irradiance Spectral Model (FISM) is an important tool for estimating solar variability for a myriad of space weather research studies and applications, and FISM Version 2 (FISM2) recently was released. FISM2 is an empirical model of the solar ultraviolet irradiance created to fill spectral and temporal gaps in the satellite observations. FISM2 estimates solar ultraviolet irradiance variations due to the solar cycle, solar rotations, and solar flares. The major improvement provided by FISM2 is that it is based on multiple new, more accurate instruments that have now captured almost a full solar cycle and thousands of flares, drastically improving the accuracy of the modeled FISM2 solar irradiance spectra. Specifically, these new instruments are SDO EVE, SORCE XPS, and SORCE SOLSTICE. FISM2 is also improved to 0.1 nm spectral bins across the same 0-190 nm spectral range, and is already being used in research to estimate space weather changes due to solar irradiance variability in planetary thermospheres and ionospheres.

1 Introduction

The Flare Irradiance Spectral Model (FISM) (Chamberlin et al., 2007, 2008), released in 2005, is an empirical model of the solar ultraviolet spectral irradiance from 0-190 nm created to fill spectral and temporal gaps in actual measurements. FISM estimates solar ultraviolet irradiance variations due to solar cycle, solar rotation, and solar flare variations. The original release of FISM, hereafter referred to as FISM1, has been used in numerous studies to more accurately quantify the influence of the aforementioned solar variations on planetary ionospheres and thermospheres at Earth (Qian et al., 2010, 2011, 2012) and at Mars (Lollo et al., 2012). FISM1 has also been used to study lunar dust charging (Sternovsky et al., 2008; Harada et al., 2017), photoelectron production at Earth and Mars (Peterson et al., 2009, 2012, 2013; Xu et al., 2015), and estimate the amount of Total Solar Irradiance (TSI) energy radiated during solar flares (Emslie et al., 2012; Moore et al., 2014). FISM1 empirical relationships were also used as the basis for the development of the Mars Atmosphere and Volatile Experiment (MAVEN) (Jakosky et al., 2015) EUV Monitor (EUVM) FISM-M model (Eparvier et al., 2015; Thiemann, Chamberlin, et al., 2017).

Since the release of FISM1, a new suite of improved solar irradiance instruments has been launched, many of which were optimized with the cadence and duty cycle to fully measure the spectral and temporal evolution of solar flares. These instruments are the Extreme-ultraviolet Variability Experiment (EVE) (Woods et al., 2012), the Solar Stellar Irradiance Comparison Experiment (SOLSTICE) (McClintock et al., 2005), and the X-ray Photometer System (XPS) (Woods, Rottman, & Vest, 2005). Version 2 of FISM, FISM2, is now released and is based on these new, more accurate and more numerous measurements that have now captured almost a full solar cycle and thousands of flares, drastically improving the accuracy of the modeled FISM2 solar irradiance spectra. FISM2 is improved to 0.1 nm spectral bins across the same 0-190 nm spectral range. FISM2 is currently available through the LASP Interactive Solar Irradiance Datacenter (LISIRD; `http://lasp.colorado.edu/lisird`) or for direct file downloads at `http://lasp.colorado.edu/eve/data_access/evewebdata/fism/`.

FISM2 is available in two products with different temporal cadences: a 'daily' and a 'flare' product. The 'daily' product contains a single spectrum for each day and models the solar cycle and solar rotation irradiance variations. The 'flare' product has one spectrum every 60 s, and starts with the daily product and then includes additional variations due to solar flares. The 'daily' and 'flare' products are available in either the 0.1 nm spectral binning across the spectra range, or pre-binned into the 23 'Stan Bands' (Solomon & Qian, 2005) to ease direct input of FISM2 spectra into atmospheric models that use these bins as standard such as the Whole Atmosphere Community Climate Model (WACCM) (Marsh et al., 2013; Hurrell et al., 2013). FISM2 data is also adjusted to a constant dis-

tance at 1AU, similar to the measurements it is based on, so those who want to use it as an input for driving planetary atmospheres, including Earth's, would need to adjust it for the orbital distance and eccentricities of the planet they are studying.

This paper describes the details of the FISM2 algorithms and presents a small subset of the results. Section 2 describes the new measurement data sets that FISM2 uses as basis for its empirical modeling. The algorithms that are used in the empirical model are then presented in Section 3, while results of FISM2 as well as comparisons to the base data sets are then given in Section 4.

2 Data Sets Used in FISM2

The primary FISM2 upgrade is the use of newly available, long-term measurement data sets, many of which have improved spectral resolution, cadence, and accuracy over the measurements used as the basis for FISM1. These data sets described in this section are provided at 0.1 nm or better spectral resolution that FISM2 will model.

2.1 The EUV Variability Experiment (EVE)

EVE (Woods et al., 2012) is one of three instruments that was launched on-board the Solar Dynamics Observatory (SDO)(Pesnell et al., 2012) on 11 February 2010, and the EVE science data products start on 28 April 2010. EVE measures the solar ultraviolet spectral irradiance using multiple channels to cover its entire spectral range. The Multiple EUV Grating Spectrographs A and B (MEGS-A and MEGS-B) are the primary channels, with MEGS-A covering a spectral range from 6-37 nm and MEGS-B covering the range from 35-105 nm, both at 0.1 nm spectral resolution and around 10% accuracy. MEGS-A operated at nearly 100% duty cycle, producing a spectrum every 10 s until it was lost on 26 May 2014 due to a power anomaly with its electronics. MEGS-B is presently still operational, but at a reduced duty cycle of only 3 hours each day due to increased degradation. The EVE flight software was updated to start this 3 hour window when the GOES-XRS B-channel and its derivative reach a certain threshold approximately at a NOAA GOES flare class of M1 level. This autonomous implementation allows MEGS-B to observe flares that is would otherwise miss during its normal 3 hour daily observation. The EUV Spectral Photodiodes (ESP) (Didkovsky et al., 2012) channel contains five broadband diodes, 4 bands in the 17-38 nm range as one at 0.1-7 nm. ESP is still making nearly continuous measurements, besides some planed nominal calibrations, and is available at 0.25 s cadence.

The EVE duty cycle has allowed it to measure thousands of flares through their complete temporal evolution during its mission of C-class or higher. The 0.1 nm spectral resolution has also isolated many of the emission lines to reduce blends, given the many emission lines that are present throughout the ultraviolet spectrum, further improving the FISM2 modeling. EVE measurements are a significant improvement over the Solar EUV Experiment (SEE) (Woods, Eparvier, et al., 2005) used as the basis in the EUV wavelengths for FISM1. SEE only observed 27 flares by the time of FISM1 release, and SEE only had 1 nm spectral resolution with many emission line blends. EVE also has much improved accuracy of its measurements over SEE, especially during solar flares, which along with the improved statistics with the thousands of events leads to much more accurate FISM2 products. FISM2 is based on the EVE Level 2, Version 6 data products.

2.2 The Solar Stellar Irradiance Comparison Experiment (SOLSTICE)

SOLSTICE (McClintock et al., 2005) was launched on the Solar Radiation and Climate Experiment (SORCE) (G. Rottman, 2005) on 25 January 2003. SOLSTICE is a scanning spectrometer that measures the far ultraviolet solar spectral irradiance from

115-320 nm. The daily median variations for FISM1 Far Ultraviolet (FUV) wavelength range from 115-190 nm were based on the previous version of SOLSTICE that flew on board the Upper Atmosphere Research Satellite (UARS) (G. J. Rottman et al., 1993). With more than a solar cycle observed (over fifteen years) by SORCE/SOLSTICE, including many flares measured, the SORCE version of SOLSTICE is used as the base measurement set for FISM2. In addition to the daily data, SORCE/SOLSTICE measurements will also be used for the flare variations in FISM2. The FISM1 flare variations were based on TIMED/SEE due to the difficulties of data reduction of the SOLSTICE scanning spectrometer measurements, but this effort was completed for FISM2 and has led to more accurate, higher spectral resolution model estimates of the FUV flare variations. FISM2 is based on the SOLSTICE Level 3, Version 15 data products.

2.3 The X-ray Photometer System (XPS)

The XPS (Woods, Rottman, & Vest, 2005) on board the SORCE satellite is used for FISM2 in the soft X-ray wavelength range from 0.1-6 nm. The SORCE version of XPS is preferable to the TIMED XPS because of its much higher duty cycle. XPS is a set of broadband diode measurements from 0.1-27 nm that are each 5-7 nm wide, but an algorithm was developed that uses the XPS diode measurements to drive the Chianti model (Dere et al., 1997, 2009) in order to produce a spectrum at higher spectral resolution. This XUV spectral model is calculated at each of the XPS measurements (Woods et al., 2008), and the product is at 0.1 nm bins ranging from 0.1-40 nm and served as the Version 11, Level 4 SORCE/XPS data product. This XPS L4 model is what is used as the base measurements in the FISM2 0-6 nm range. The reference spectra used in the XPS L4 algorithm are being updated based on the EVE and Miniature X-ray Solar Spectrometer (MinXSS) (Mason et al., 2016, 2020) CubeSat observations, and once released will be included into FISM2.

2.4 FISM2 Proxies

Empirical models rely on proxies, a small set of measured quantities that represent similar variations as those being modeled across the entire spectral range. Many of the proxies for FISM2 are similar to those in FISM1 and are established data sets with a long history, few data gaps, and continued planned support for future measurements. The daily-averaged proxies represent changes in the solar irradiance driven by the approximately 11-year solar cycle and the approximately 27-day solar rotation and active region evolution. The proxy that allows FISM2 daily estimations to go back as far as 1947 is the Penticton 10.7 cm radio flux, or F10.7, adjusted to 1AU (`https://www.spaceweather.gc.ca/solarflux/sx-en.php`). This is usually measured three times per day, and the lowest of the three is used to filter out any large radio bursts that are present in the data as well as minimize the chance that the higher two are observed during solar flares.

Two other daily-averaged proxy data sets are the Mg II core-to-wing ratio (MgII c/w) (Snow et al., 2005) and H I Lyman-α emission line at 121.6 nm (Lyα). These proxies best represent solar variations in emissions from in the chromosphere and transition regions of the solar atmosphere. The MgII c/w proxy comes from the Bremen composite data set that dates back to 1978 (`http://www.iup.physik.uni-bremen.de/gome/gomemgii.html`) while the Lyα composite comes from a compilation of measurements assembled and adjusted for consistency by Woods et al. (2000) back to 1981 and is available here (`http://lasp.colorado.edu/data/timed_see/composite_lya/composite_lya.dat`). Note that some versions of the Mg II and Lyα composite indices do empirical modeling using F10.7 to fill their own gaps between available measurements. Those modeled Lyα and Mg II results are not used in FISM, only the ones where actual measurements are made and available. Gaps in the F10.7 index are filled and used, though, to provide a complete index set for every day back to 1947, so no gaps will exist in the FISM2 daily product.

Other 'daily' proxies are also used that are beginning to compile a long data set and also have future planned measurements. These include the 17.1 nm and 30.4 nm emission lines from SDO/EVE, as well as a soft X-ray band from 0-7nm. The 0-7nm continua representing the hot corona Bremsstrahlung continuum. The 17.1 nm is from the Fe IX emission line formed around 800 MK that represents the cool corona. The He II 30.4 nm emission proxy is cooler emission formed around 80,000 K, and represents emission lines formed in the chromosphere. These proxies have both been measured since 2001 from TIMED SEE, while have also been continued through SDO/EVE in both the MEGS-A channel, from 2010-2014, as well as from the ESP channel on EVE from 2001-present. Hopefully the ESP 0-7 nm, 17.1 nm and 30.4 nm proxies and MEGS-P 121.6 nm Lyα measurements from EVE will continue long into the future, while the 30.4 nm, 121.6 nm, and Mg II c/w proxy measurements, along with many other new EUV proxies, will be continued long into the future on the new GOES EUVS instrument.

A statistical analysis was done for each wavelength bin to find which single daily proxy most accurately represented each given wavelength, as was done for FISM1. When the optimal proxy is not available, the next best available proxy from the statistical analysis is then used. Every modeled wavelength ends up using the F10.7 proxy, as it is the only one available every day since 1947 and is the only proxy available prior to the onset of MgII c/w and Lyα that became more routinely available in 1978. The most recent estimates have the best set and most representative proxies, and therefore will have the most accurate solar irradiance estimates.

The flare proxies that are used in FISM2 are currently the same as were used for FISM1, the 'long' or 'B' channel of the X-ray Spectrometer (XRS; (Garcia, 1994; Chamberlin, Woods, Crotser, et al., 2009)) on the Geostationary Operational Environmental Satellites (GOES), as well as the time derivative of the XRS-B channel. The irradiance values that are used are the operational products that do not contain any 'correction factor' that has been found to convert the available NOAA data product to the 'science' irradiance values with accurate W/m^2/nm. The XRS-B measurements represent the thermal, gradual phase of the solar flare, while its derivative represents the non-thermal impulsive phase of the solar flare that was first described by Neupert (1968, 1989).

3 FISM2 Algorithms

FISM2 empirical model algorithms are largely similar to those in FISM1 (Chamberlin et al., 2007, 2008). FISM2 is made up of the sum of five components, starting with the base solar minimum reference spectrum, E_{min}, and then adding onto it the irradiance variability associated with the solar cycle, E_{SC}, and solar rotation, ESR, as well as the two solar flares components due to the gradual, E_{GP}, and impulsive phase, E_{IP}, variations. All five of these contributions are modeled independently. The FISM2 daily model that determines the solar spectral irradiance, E, at wavelength 'λ' on day 'd' is

$$E_{daily}(d,\lambda) = E_{min}(\lambda) + E_{SC,Mod}(d,\lambda) + E_{SR,Mod}(d,\lambda) \quad (1)$$

There is only a single solar minimum reference spectrum for all days and times, hence it has no 'd' dependence. There is one full spectrum, from 0-190 nm at 0.1 nm bins, produced for each day, d, in the daily model. There is not a more accurate time of day associated with the daily 'd' spectrum represents, as it depends on when the proxy used to model the irradiance was measured. Although F10.7 is usually a combination of 1-3 measurements taken around local noon in Penticton, British Columbia, most other proxies are daily averages of multiple measurements throughout the day.

The FISM2 flare model that follows finds the irradiance at 60 s cadence each wavelength at time 't' on day 'd' is

$$E_{Flare}(t,\lambda) = E_{daily}(t,\lambda) + E_{GP,Mod}(t,\lambda) + E_{IP,Mod}(t,\lambda) \quad (2)$$

where

$$E_{daily}(t,\lambda) = Spline[E_{daily}(d-2:d+2,\lambda)] \quad (3)$$

If a single daily value on day, d, was used at all times, t, as the daily component contribution in the higher-cadence flare model, significant 'steps' will occur at the midnight day boundary when going from one day to the next. To eliminate these daily boundary steps for the high-cadence flare model component, the IDL cubic spline interpolation, 'spline.pro', is used. This interpolates the 5 single daily values, $E_{daily}(d,\lambda)$ at each wavelength, from $d-2$ *days* to $d+2$ *days*, onto the higher cadence time grid is used at all times, $E_{daily}(t,\lambda)$, on day d in the FISM2 flare model. A spline is used as it provides a smooth continuous function over all days that is more representative than linear interpolations, and accounts for interpolations that are increasing, decreasing, or both multiple times within the 5 days the spline is calculated over. The standard cadence, t, for FISM2 is 60 s, but improvements are planned to provide these as rapid as 2 or 3 s upon request, based on the native cadence of the GOES XRS proxy measurements at the time of flare requested.

3.1 Solar Minimum Reference Spectrum

The solar minimum reference spectrum, E_{min}, is determined using two different methods, both using the 108-day smoothed time series for each wavelength. The first, preferred way, is for those measurements on the SORCE satellite, from SOLSTICE and XRS instruments, that observed through the entirety of the solar cycle minimum between Solar Cycles 23 and 24. The solar cycle minimum spectrum, E_{min} is then just the minimum value for each wavelength of the 108-day smoothed time series. The 108-day average is used as it was in FISM1 (Chamberlin et al., 2007), as it was determined in its analysis that this most accurately reduces the uncertainties between measurements and FISM solar cycle model estimations.

A different method is used to determine the solar minimum reference spectrum for the wavelengths represented by SDO/EVE as it started observations just after the start of Solar Cycle 24 and have not yet made (MEGS-B and ESP) or will not make (MEGS-A) observations during the minimum of Solar Cycles 24 and 25. This is the same method that was used to determine the minimum reference spectrum in FISM1, as SEE had not yet observed during solar minimum conditions. A linear fit is determined of a 108-day smoothed proxy to the 108-day smoothed measurements at each wavelength, when cotemporally observed. This linear fit is then solved for 108-day smoothed minimum value of the proxy to determine what the measurement would have been if it was observing during solar minimum time. The proxy used is the MgII c/w index, as it is degradation independent and does not have the issue that F10.7 has where it reaches its minimum value while other EUV wavelengths continue to decrease further, or F10.7 'bottoms-out' early before true solar minimum.

Given these two methods, the FISM2 solar minimum reference spectra is not a given measured or modeled spectrum on any given day or time as has been done for previous reference spectra (Chamberlin, Woods, Eparvier, & Jones, 2009; Woods et al., 2009), but rather the minimum for each wavelength regardless of when it occurred. Having different formation temperatures, different wavelength minima occur at different dates, so the full minimum reference spectra is one that may not ever actually occur.

3.2 FISM2 Solar Cycle

The solar cycle variations modeled in FISM2 use the 108-day smoothed value of the proxies and measurements and represents the approximately 11-year solar cycle. 108-day smoothing, which is equivalent of averaging over four 27-day average solar rotations, two previous and two future, is used based on a previous study done for FISM1 that demonstrated the 108-day smooth provides the lowest uncertainties in modeling the measurements of this component (Chamberlin et al., 2007). This 108-day smooth, or center average, for both the measured irradiance, $E_{SC,Meas}(d,\lambda)$, and each of the proxies, $E_{SC,P}(d)$, is given by

$$E_{SC}(d,\lambda) = \frac{\sum_{d-54}^{d+54} E(d,\lambda)}{108} - E_{Min}(\lambda) \tag{4}$$

where the solar minimum reference spectrum at each wavelength, $E_{Min,Meas}(\lambda)$, or measured proxy minimum, $E_{Min,P}(\lambda)$ is also subtracted off so that it is pure solar cycle variations that are zero at solar minimum. The best-fit relationship found is a linear fit between the measurement, $E_{SC,Meas}(d,\lambda)$, at each wavelength and each proxy, $E_{SC,P}(\lambda)$, given as

$$E_{SC,Meas}(d,\lambda) = A_{SC}(\lambda) + B_{SC}(\lambda) * E_{SC,P}(d) \tag{5}$$

This fit is to determine the linear fit coefficients, $A_{sc}(\lambda)$ and $B_{sc}(\lambda)$, using the data set for every day when both the measurement and the proxy are measured. Once these linear relationship are found for every proxy and wavelength, then the modeled irradiance for the solar cycle component, $E_{SC,Mod}(d,\lambda)$, can be determined using the know coefficients at any day the proxy is measured, or

$$E_{SC,Mod}(d,\lambda) = A_{SC}(\lambda) + B_{SC}(\lambda) * E_{SC,P}(d) \tag{6}$$

For the near-real-time estimations, when a 108-day centred' average can not be found, the previous 54-days, plus whatever days after that are available, are used to determine the average for that day. Reprocessing is done for every day in the past 60 days for two reasons, 1) to update the solar cycle proxy to the most accurate 108-day centered average that includes the averaging over the two solar rotations following it, and 2) to include any recent updates, calibrations, reprocessing, and trending to the proxies that may occur over 60 days since the measurement/proxy was taken to ensure FISM2 is using the most accurate proxies at any given time.

An example of the solar cycle fit for the EVE 30.35 nm wavelength bin, $E_{SC,Meas}(d, 30.35nm)$, using the MgII c/w proxy, $E_{SC,MgII}(d)$, (left) and the 17.1 nm proxy, $E_{SC,17.1nm}(d)$, (right) are shown in Fig. 1. These plots shows a point for every day that both EVE and MgII or 17.1 nm were measured, where the 17.1 nm proxy shown here is from the SDO/EVE/MEGS-A measurement. The solid lines show the linear fit to the respective collection of points to determine $A_{SC}(30.35\ nm)$ and $B_{SC}(30.35\ nm)$ for the respective proxies. The tailing off of the black points at high values is likely due to uncorrected degradation trends in the EVE V6 data set, as it is there in all proxies, so these points are eliminated from the fit and only the subset of red points are used. This degradation will likely be corrected in the EVE V7, so when this data set is incorporated and FISM2 fits reprocessed hopefully the entire data set can be used. There are only moderate departures from the fit on the left panel of Fig. 1, which uses a proxy, MgII, formed at a similar formation temperature, and therefore a similar region of the solar atmosphere, as the emission line being modeled, in this case the He II 30.34nm line. Futher departures from the linear fit when using a proxy of a much different formation temperature then the emission lines being modeled, as seen in the right panel when using the hotter 17.1 nm cool corona proxy to model the He II 30.34 nm choromospheric emission.

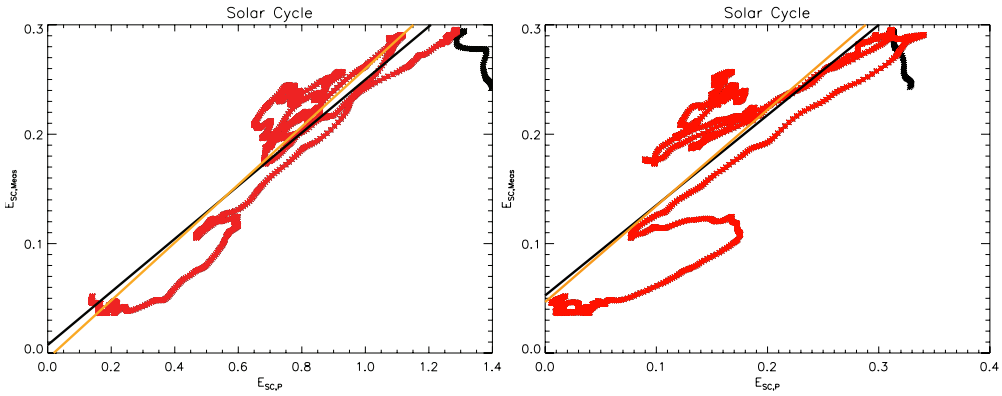

Figure 1. The solar cycle fits of the 108-day smoothed solar cycle proxy, $E_{SC,P}$, and the solar irradiance measurements, $E_{SC,Meas}$, for every day that both are measured. The fits are shown for the 30.35 nm emission bin measured by SDO/EVE compared to the MgII c/w proxy on the left and the 17.1 nm proxy on the right. The Red points are the ones used in the actual FISM2 solar cycle fit, shown by the orange line, while the black points are eliminated due to uncorrected degradation in the EVE data product. The black line represents the fit to the black points, or what the fit would have been if the bad data had not been eliminated.

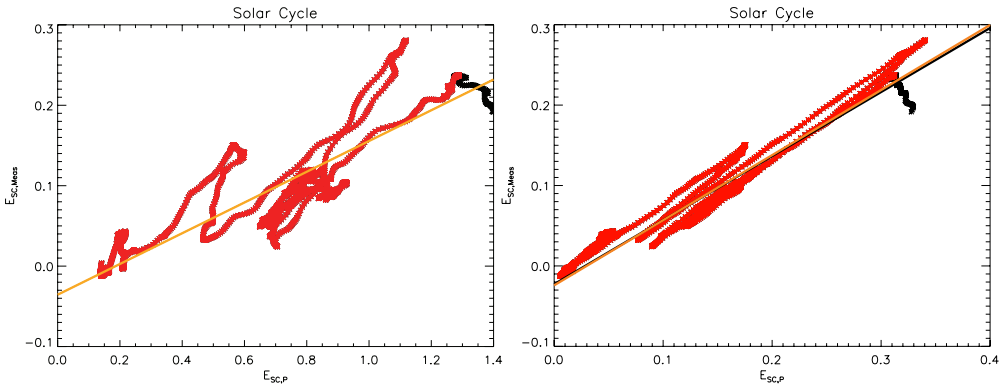

Figure 2. The solar cycle fits between the 108-day smoothed solar cycle proxy, $E_{SC,P}$, and the solar irradiance measurements, $E_{SC,Meas}$, for every day that both are measured. The fits are shown for the 17.15 nm emission bin measured by SDO/EVE compared to the MgII c/w proxy on the left and the 17.1 nm proxy on the right. The Red points are the ones used in the FISM2 solar cycle fit, shown by the orange line, while the black points are eliminated due to uncorrected degradation in the EVE data product. The black line represents the fit to the black points, or what the fit would have been if the bad data had not been eliminated.

Similarly, when showing the 17.1 nm cool corona emission line modeled by both the MgII proxy (left) and the 17.1 nm proxy (right), Fig. 2 shows that this time the 17.1 nm is obviously the best proxy and the cooler MgII proxy shows the large departures from linear fit. These figures demonstrate the need for a range of proxies, with different formation temperatures spanning those present in the solar atmosphere, are needed to most accurately empirically model the complete solar ultraviolet spectrum, as is done in FISM2.

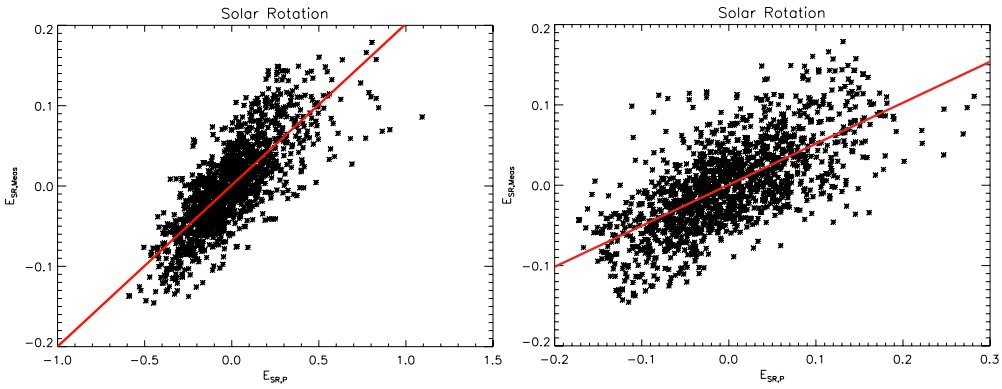

Figure 3. The FISM2 solar rotation model fits, shown as the red line, between the solar rotation proxy value, $E_{SR,P}$ and the solar rotation measurement, $E_{SR,Meas}$. This example is for the 30.35 nm bin measured by SDO/EVE fit to two different proxies, p, the MgII c/w proxy (left) and 17.1 nm proxy (right).

3.3 FISM2 Solar Rotation

The solar rotation component, $E_{SR}(d,\lambda)$, for both the measurements and the proxies, is then the residual of the daily measured irradiance value and the solar cycle 108-day smoothed value, or

$$E_{SR}(d,\lambda) = E(d,\lambda) - \frac{\sum_{d-54}^{d+54} E(d,\lambda)}{108} \tag{7}$$

The FISM2 solar rotation component of the model is again a linear fit of the measurements at each wavelength, $E_{SR,Meas}(d,\lambda)$, and the proxies for the corresponding days, $E_{SR,P}(d)$, given as

$$E_{SR,Meas}(d,\lambda) = A_{SR}(\lambda) + B_{SR}(\lambda) * E_{SR,P}(d) \tag{8}$$

As with the solar cycle component, once the linear fit coefficients, $A_{SR}(\lambda)$ and $B_{SR}(\lambda)$, are calculated between all the co-temporal measurements for each wavelength and the proxy, the modeled irradiance, $E_{SR,Mod}(d,\lambda)$, for each wavelength can be found any day, d, the proxy is available, or

$$E_{SR,Mod}(d,\lambda) = A_{SR}(\lambda) + B_{SR}(\lambda) * E_{SR,P}(d) \tag{9}$$

An example of the solar rotation fit is shown in Fig. 3, again for the 30.35 nm wavelength bin and the MgII c/w (left) and 17.1 nm (right) proxies. As can be seen this solar rotation component varies around zero due to the subtraction of the 108-day average solar cycle component. Again, the proxy with the most similar formation temperature as the emission it is modeling. In this case, using the MgII proxy to model the He II 30.4nm chromospheric emission line shows a much tighter fit; therefore, it has much lower 1σ uncertainties associated with it and provides a more accurate model in this bin.

A similar solar rotation fit example is shown in Fig. 4, this time using the cool corona 17.1 nm emission line and again using the MgII solar rotation proxy on the left and the 17.1 nm proxy on the right. This example exemplifies using a similar temperature proxy,

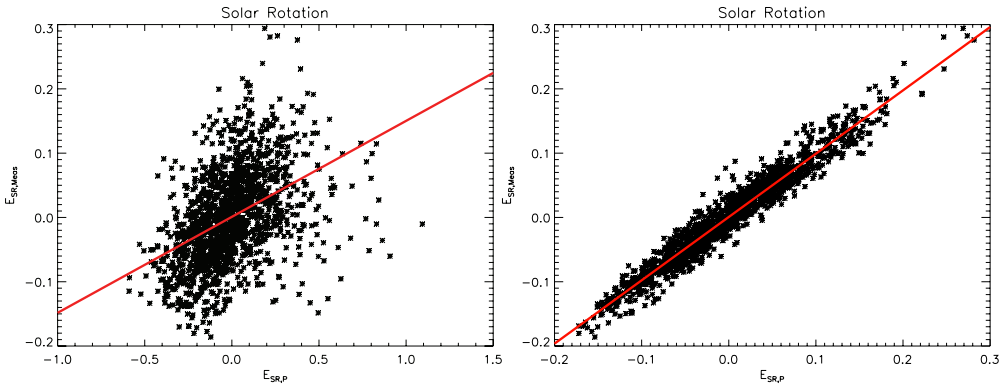

Figure 4. The FISM2 solar rotation model fits, shown as the red line, between the solar rotation proxy value, $E_{SR,P}$ and the solar rotation measurement, $E_{SR,Meas}$. This example is for the 30.35 nm bin measured by SDO/EVE fit to two different proxies, p, the MgII proxy (left) and 17.1 nm proxy (right).

where the points are very tightly fit to the model line, meaning it has very low associated 1σ uncertainties in this component. The MgII proxy can be used, and is used when the 17.1 nm proxy is unavailable (e.g from 1978 until 2001 when TIMED SEE started), but the uncertainties are much larger when having to use the proxy with a much different formation temperature.

The uncertainties of the daily model, which includes the solar cycle and solar rotation components, will be discussed later in Sec 3.7. The daily model uncertainties are calculated as the standard deviation of the end model daily product to the actual daily measurements, when the measurements are available.

3.4 FISM2 Impulsive Phase

The FISM2 solar flare components are broken up into two phases, as was done for FISM1. Most of the hottest flare emissions, those at $log(T) > 6.8$, in the ultraviolet wavelength range only show a gradual phase component, while many of the emissions formed in the solar chromospheric and transition region are dominated by their impulsive phase component. The impulsive phase proxy, $E_{IP,P}(t)$, is the positive time derivative of the GOES XRS-B channel, $E_{Meas,XRS}(t)$, represented by the "Neupert Effect" (Neupert, 1968, 1989) that shows the relationship between the non-thermal energy input in the lower atmosphere during a flare and the resultant thermal plasma that is created and measured by the XRS soft X-ray plasma emissions, or

$$E_{IP,P}(t) = \frac{dE_{Meas,XRS}(t)}{dt} \geq 0.0 \tag{10}$$

The impulsive phase measurements from XPS, EVE, or SOLSTICE, $E_{IP,Meas}(t)$, are the measurement at time, t, minus the daily median measurement for the day. For EVE and XPS, there is only one measurement/proxy data point used for each flare, and it is always at the peak time of the impulsive phase, t, determined from the time of the peak time derivative of the GOES XRS-B data during the flare. This is demonstrated for a single flare in Fig. 5 by the green circles. This is shown for two wavelengths, the He II cooler emission that is dominated by the impulsive phase emissions (left panel) and a hot Fe XX 12.18nm emission line that is dominated by the gradual phase.

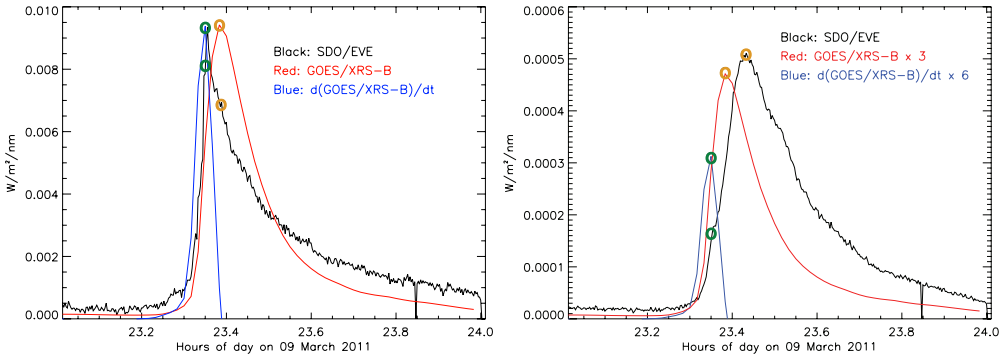

Figure 5. Two examples of the measurement and proxy values that are selected when building up the flare database. The left figure shows an emission that is dominated by the impulsive phase, which is the He II 30.34 nm emission from SDO/EVE (black). Also shown are the two flare proxies, GOES/XRS-B (Red, scaled by a factor of 60), and its time derivative (Blue, scaled by 180). The impulsive phase proxy and measurement values for each of the wavelengths are given by the green circles, while the gradual phase ones are given by the orange circles. The right plot shows the Fe XX emission at 12.18 nm (black), so is dominated by the gradual phase that peaks after the GOES XRS-B time series; therefore, the peak value following the GOES peak is then used, while the impulsive phase proxy and measurement values are always at the same time. In this panel, the GOES/XRS-B (red) is scaled by a factor of 3 and the dGOES/dt (blue) is scaled by a factor of 6.

For EVE wavelengths, the data set is then built up using all flares C5 or above in the EVE data set from the start of the EVE mission (May 2010) to the failure of MEGS-A (May 2014). For the XPS wavelengths, all co-temporal data points are used where the GOES XRS-B time derive is above 1e-8 during the SORCE mission are used. For SOLSTICE, the cotemporal data points are fit where the GOES XRS-B time derivative is above 1e-10 during solstice measurements. The impulsive phase equation to relate to the measurements to the above impulsive phase proxy, $E_{IP,P}(t)$, is a power law relationship, same as it was for FISM1 (Chamberlin et al., 2008)

$$E_{IP,Meas}(t,\lambda) = E_{Meas}(t,\lambda) - E_{Meas}(d,\lambda) \tag{11}$$

and

$$E_{IP,Meas}(t,\lambda) = A_{IP}(\lambda) * E_{IP,P}(t)^{B_{IP}(\lambda)} \tag{12}$$

The uncertainties attributed to the impulsive phase component is the 1σ uncertainties of this fit. Once the impulsive phase power law coefficients are found, the impulsive phase contributions to the modeled irradiance, $E_{IP,Mod}(t,\lambda)$, can be found when the XRS time derivative proxy is available and positive by

$$E_{IP,Mod}(t,\lambda) = A_{IP}(\lambda) * E_{IP,P}(t)^{B_{IP}(\lambda)} \tag{13}$$

This power law fit is found using the Interactive Data Language (IDL) 'poly_fit.pro' routine, which is a least-squares polynomial fit. In order to use this routine, the natural logarithm is taken of Eq. 13, or

$$ln[E_{IP,Mod}(t,\lambda)] = ln[A_{IP}(\lambda)] + B_{IP}(\lambda) * ln[E_{IP,P}(t)] \quad (14)$$

which then puts it in a simple linear function to be fit.

There are actually four different fits performed, based on the flare location on the solar disk, in order to quantify the center-to-limb variability that corrects for optically thick emissions being modeled by an optically thin GOES XRS-B proxy, and will be discussed further in Sec. 3.6. The fits are performed for 'all' flares as well as subsets of 'center' flares, which have a flare location, fl_{loc} that is within 45°of disk center, 'mid' where flares are between 45°and 75°, and 'limb' flares are between 75°and 90°, and fl_{loc} is defined using the flares latitude, fl_{lat}, and longitude, fl_{lon}, defined by the NOAA Space Weather Prediction Center in its Solar Event Reports, as:

$$fl_{loc} = \sqrt{(fl_{lat})^2 + (fl_{lon})^2} \quad (15)$$

This flare location is the flare intensity centroid derived using solar images from the NOAA Solar UltraViolet Imagers (SUVI), while future FISM2 flare locations will be derived from the new GOES-16$^+$ XRS capabilities for flare location (Chamberlin, Woods, Eparvier, & Jones, 2009).

Example fits, solid lines, along with the two of the plus 1σ deviation of the fits, dashed lines, are shown on the left in Fig. 6 for the 10.25 nm wavelength bin containing the strong Fe XXI emission line at 10.22 nm, which is a hot flare line formed at a temperature of around 15 MK. Given that this bin is dominated by a hot, optically thin emission line, the actual modeled irradiance change due to the impulsive phase is relatively small, and the center, mid, and limb fits are all approximately the same (note the green 'limb' fit is the same as the black 'all' flare fit for this bin). Regardless, there is still a slight, significant separation and center-to-limb (CTL) darkening found, as is the case in most hot lines observed by SDO/EVE in the FISM2 analysis, even the very hot flare emissions as is expected based on the results from Thiemann et al. (2018). The FISM2 impulsive phase fit for an optically thick line is also shown on the right side of Fig. 6. This is for the 30.35 nm wavelength bin containing the strong He II 30.38 nm emission line formed in the solar chromosphere. Here the magnitude of the impulsive phase irradiance increase is dramatic, and the separation of the fits to the center (red), mid (blue), and limb flares (green) are clearly shown and distinguished from each other, which allows the CTL correction to be quantified and corrected for using the optically thin GOES XRS soft X-ray proxy.

The FISM2 Impulsive Phase power law fits only apply to EUV and FUV wavelengths, as in those wavelengths above 6 nm. For the 0-5 nm XUV range, no significant impulsive phase contributions were found. This is expected as this range consists of hot emission lines and free-free continuum emissions that are expected to be dominated by the thermal gradual phase, but it also may be due to the SORCE/XPS L4 observations and model themselves, and also that the cadence of these data are at 5 minutes and may average out the sharp impulsive phase peaks.

3.5 FISM2 Gradual Phase

The gradual phase proxy is the GOES XRS-B channel. The FISM2 gradual phase relationship, as it was for FISM1 (Chamberlin et al., 2008), is a power law relationship for EUV to FUV wavelengths above 6 nm, and a simple linear relationship for XUV wavelengths below 6 nm. These fits are found for each wavelength, λ, between the high cadence flare measurement at time t, $E_{Meas}(t^*, \lambda)$, minus its daily value for day 'd', $E_{Meas}(d, \lambda)$, to represent only the flare changes, and the GOES XRS-B high time cadence flare measurement, $E_{P,GP}(t)$, shown here

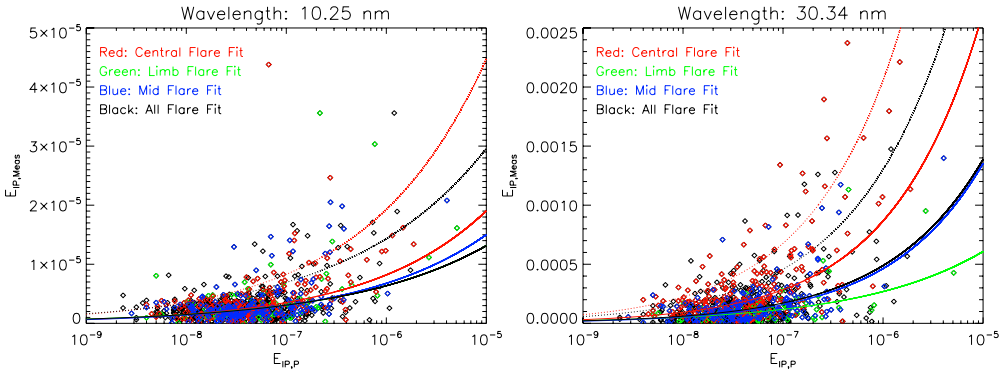

Figure 6. The FISM2 Impulsive Phase flare fits, shown as solid lines, for two wavelength bins containing strong emission lines: the 10.25 nm bin containing the hot 10.22 nm emission formed in the corona (left) and the 30.35 nm bin containing the cool He II 30.38 nm emission line formed in the chromosphere (right). The fits are done for all flares (black), as well as those located in the center of the solar disk (red), defined as within 45° of disk center, mid (blue) flare located between 45° and 75° of disk center, and limb (green) flare located between 75° and 90°. The $+1\sigma$ fits are also shown for the 'all' and 'center' fits as dashed lines of the respective color.

$$E_{GP,Meas}(t^*,\lambda) = E_{Meas}(t^*,\lambda) - E_{Meas}(d,\lambda) \tag{16}$$

$$E_{GP,Meas}(t^*,\lambda) = A_{GP}(\lambda) * E_{GP,P}(t)^{B_{GP}(\lambda)} \; for \; 6-190 \; nm \tag{17}$$

$$E_{GP,Meas}(t^*,\lambda) = A_{GP}(\lambda) + B_{GP}(\lambda) * E_{GP,P}(t) \; for \; 6-190 \; nm \tag{18}$$

As was done for the impulsive phase, the natural logarithm of the power law equation is taken to produce a linear equation that is actually fit. Given that flare energy release is a process that heats the solar flare plasma to more than 10 MK (Caspi & Lin, 2010), the plasma then cools over time (Cargill et al., 1995). Therefore, the many emission lines radiate at different times as the plasma cools into temperatures with their characteristic contribution function, and peak at different times (Ryan et al., 2013; Thiemann, Eparvier, & Woods, 2017); therefore, only the peak irradiances for each flare at times t^* are used and fit compared to the peak GOES XRS-B irradiance at time t. This is shown by the orange circles in Fig. 5. Time t^* is found to be the time of the peak irradiance for each wavelength and each flare, and it must occur after the GOES XRS-B peak to avoid finding the impulsive phase flare peak.

This peak time shift is done only for wavelengths below 105 nm, as the SDO/EVE and SORCE/XPS have significant enough cadence to fully cover in the time domain to measure the full flare profile. Unfortunately for SORCE/SOLSTICE the spectral scanning means no full flare temporal profile is observed for any given wavelength, so for wavelengths > 115 nm t^* is just t, and leads to larger uncertainties in the modeling and representation of the gradual phase flare component of FISM2. The SOLSTICE scanning, as well as eclipse periods, also means that many flares are missed for any given wavelength. But given the over 16 years of solar observations the flare observations are built up to a significant database to make the FISM2 fits and derive uncertainties to these fits.

Although this time delay is used to find the flare peaks so peak irradiances of each wavelength and flare can be related to the peak GOES XRS-B irradiance, this flare delay is not implemented in the FISM2 model; therefore, all wavelengths throughout the spectrum will peak at the same time as the XRS flare time series. There are some ideas to incorporate this flare time delay for each wavelength, including using the two channels of the XRS to derive a flare plasma temperature, and then use this to determine how to shift the GOES XRS proxy, the actual implementation, testing, and validation of this correction will take significant effort so are delayed for a future FISM release.

Once the power law coefficients are known, the gradual phase contributions for FISM2, $E_{GP,Mod}(t,\lambda)$, at all wavelengths can be modeled at time t by

$$E_{GP,Mod}(t,\lambda) = A_{GP}(\lambda) * E_{P,GP}(t)^{B_{GP}(\lambda)} \tag{19}$$

As with the other FISM2 components, the uncertainty on this component is the 1σ deviation of the fit. The actual error calculation is presented later in Sec. 3.7 and given by Eq. 21. Example gradual phase fits between the GOES XRS-B proxy and the measurements are presented in Fig. 7. As described earlier, there is a single point for each flare, using the peak GOES XRS-B irradiance during the flare for the proxy value and the maximum measured irradiance value for each wavelength at its maximum time t^*, which occurs at a time after the GOES XRS-B peak. The model fits are given as solid lines, and the 1σ deviation of the 'center' and 'all' fits are shown as dotted lines. The left panel in Fig. 7 is the FISM2 10.25 nm wavelength bin containing the strong Fe XXI emission line at 10.22 nm, which is a hot flare line formed at a temperature of around 15 MK. This is a hot, optically thin emission line, so the center, mid, and limb fits are all approximately the same – in fact they are forced to be the same when close or in opposite 'center-to-limb brightening' order, and use simply the single fit to all flares regardless of flare location.

The FISM2 gradual phase fit for another, optically thick line is also shown in the right panel of Fig. 7. This is again for the 30.35 nm wavelength bin containing the strong He II 30.38 nm emission line formed in the solar chromosphere. Here the separation of the fits to the center (red), mid (blue), and limb flares (green) are clearly shown and distinguished from each other, which allows the CLV correction to be quantified and corrected for using the optically thin GOES XRS soft X-ray proxy.

It is noted that the black points in Figs. 6 and 7 do not have an associated flare location from the NOAA events database. This reduces the accuracy of the FISM2 estimations as the CLV correction can't be made so there is a much larger spread of the possible data. Getting a consistent and accurate flare location is critical to FISM2 flare increased accuracy, and the new flare location derived from the GOES-16$^+$ XRS quad diodes will assist in accurately getting this location (Chamberlin, Woods, Eparvier, & Jones, 2009).

In examining each of these fits and the dominant emission line in each 0.1 nm bin, in more cases than not a bin dominated by a hot emission line of formation temperatures $>$ 10 MK often still showed significant center-to-limb darkening. As seen in Fig. 8 is the fit for the 13.55 nm wavelength bin, which is dominated by the Fe XXII emission line formed at 15 MK and historically expected to be optically thin. But, as discussed recently in Thiemann et al. (2018), measurement from SDO/EVE have measured optically thick center-to-limb variations in flares in these hot EUV emissions, and this is modeled and characterized in FISM2 in emission lines where the fits are significant between the center and limb.

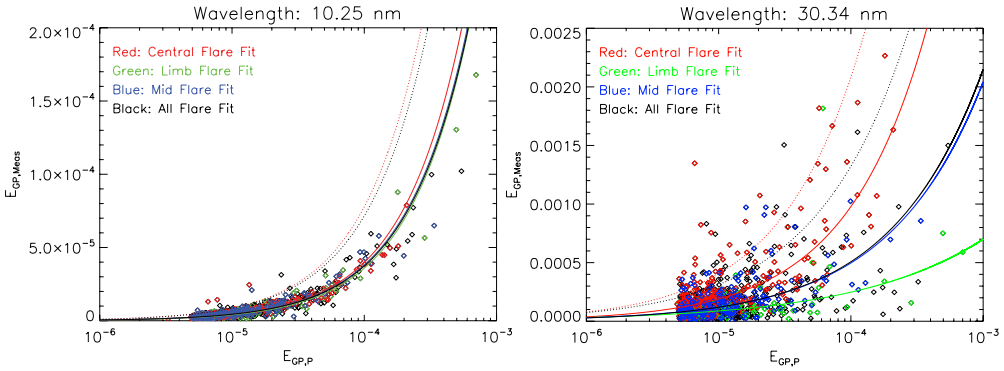

Figure 7. The FISM2 gradual phase flare fits, solid lines, for the two wavelength bins containing strong emission lines: the 10.25 nm bin containing the hot 10.22 nm emission formed in the corona (left) and the 30.35 nm bin containing the cool He II 30.38 nm emission line formed in the chromosphere (right). The fits are done for all flares (black), as well as those located in the center of the solar disk (red), defined as within 45°of disk center, mid (blue) flare located between 45°and 75°of disk center, and limb (green) flare located between 75°and 90°. The plus 1σ fits are also shown for the 'all' and 'center' fits as dashed lines of the respective color.

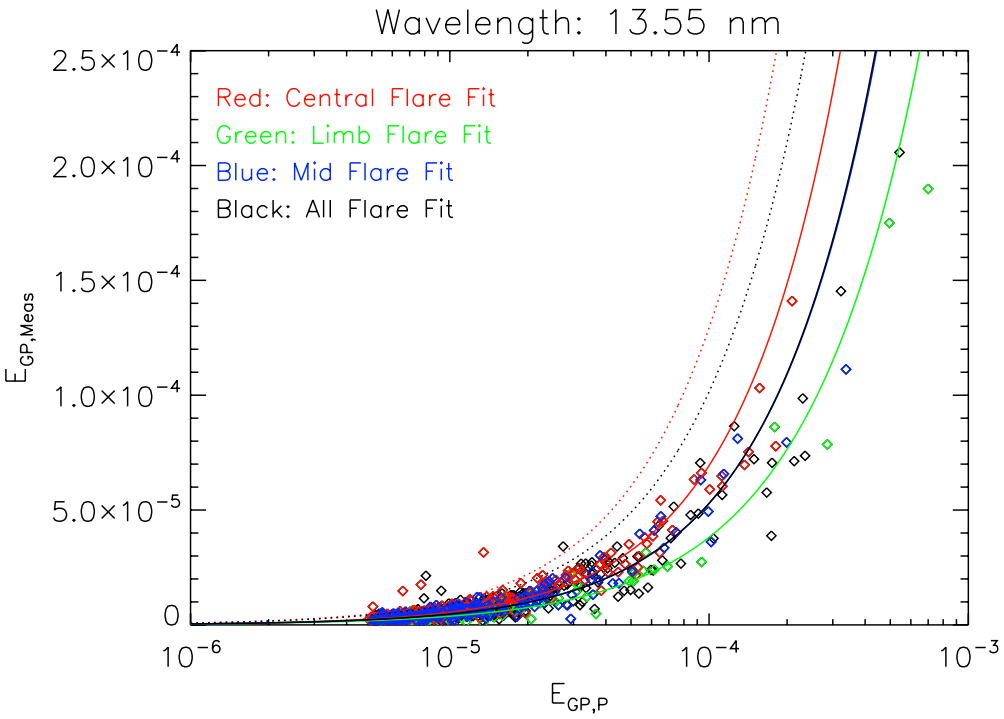

Figure 8. The FISM2 gradual phase fit for the 13.55 nm bin, containing the hot Fe XXII flare emission line. This bin shows significant center-to-limb variations, even though historically these hot emission lines have been assumed to be optically thin.

3.6 FISM2 Flare Center to Limb Variations

The flare emission for optically thick emission can be suppressed relative to the optically thin GOES XRS measurement of the flare magnitude (Chamberlin et al., 2008;

Thiemann et al., 2018; Milligan et al., 2019); therefore, the flare location is critical information to correct for these relatively reduced emissions when a flare occurs away from disk center. This FISM2 center-to-limb variation (CLV) correction is determined as it was for FISM1, but this time with a large increase in the number of flare data sets. The flare location is determined from the NOAA flare event reports, which gives latitude and longitude of the flare centroid. The hypotenuse of these two legs are then calculated to determine the angle from disk center the flare is located.

The power law fit between the flare proxy and the measured flare emission for all flares is fit separately to three different regions based on flare location to determine the CLV, those flares located $0 - 45°$ (center), $45 - 75°$ (mid), and $75 - 90°$ (limb) from disk center, as was shown in Figs. 6 and 7. A cosine correction function is then found to both the fit coefficient as well as the power law exponent using these three fits for each wavelength, that is then used to correct the irradiance increases found during a flare. This is a larger correction for the more optically thick the emission lines.

It is noted that a large number of the impulsive phase fits showed significant, although sometimes small, center-to-limb variations. This is not surprising that even though some plasma temperatures are hot, these emission are coming from the chromosphere or transition region heights, or very low in the corona where the flare-accelerated electrons initially deposit their energy early in the impulsive phase; therefore, this is evidence that even low in the solar atmosphere the plasma can reach very hot temperatures at this energy deposition site, where the higher densities cause optically thick center-to-limb variations for even some of the hottest emissions during the impulsive phase.

3.7 FISM2 Uncertainties

The FISM2 uncertainties are determined separately for the daily and flare models. The daily model uncertainties are found for each wavelength, λ, separately by calculating the relative uncertainty. This reported uncertainty finds the sum of the squares of the difference between the FISM2 daily estimates and the co-temporal measurements for which they were based on, at each day, d, or

$$\sigma_{daily}(\lambda) = \sqrt{\frac{\sum_{d=1}^{N} [\frac{E_{Mod}(d,\lambda) - E_{Meas}(d,\lambda)}{E_{Meas}(d,\lambda)}]^2}{N}} \tag{20}$$

The measurements again are the SORCE/XPS from 0-6 nm, SDO/EVE from 6-105 nm, and SORCE/SOLSTICE from 105-190 nm, and given that FISM2 is available for every day back to 1947, if there is a measurement for a day then there is a FISM2 value for the day.

For the flare model uncertainty contributions, the impulsive and gradual phase uncertainties are the relative standard deviation errors of the measurement-model differences when they are found as discussed in Secs. 3.4 and 3.5, respectively. This is similar to the daily uncertainty measurement-model calculation given in Eq. 20. Once the fits are found, the relative difference of the measurement at time, t, for the impulsive phase, and time t^* for the gradual phase, only during times of flares, is found using Eq. 21 given by.

$$\sigma_{flare}(\lambda) = \sqrt{\frac{\sum_{t=1}^{N} [\frac{E_{Mod}(t,\lambda) - E_{Meas}(t,\lambda)}{E_{Meas}(t,\lambda)}]^2}{N}} \tag{21}$$

where t=t for the impulsive phase and t=t^* for the gradual phase.

The power law fit for the FISM2 wavelength bin of 10.45 nm is shown in Fig. 9 in solid red, where the co-temporal SDO/EVE and GOES/XRS-B points that are fit are

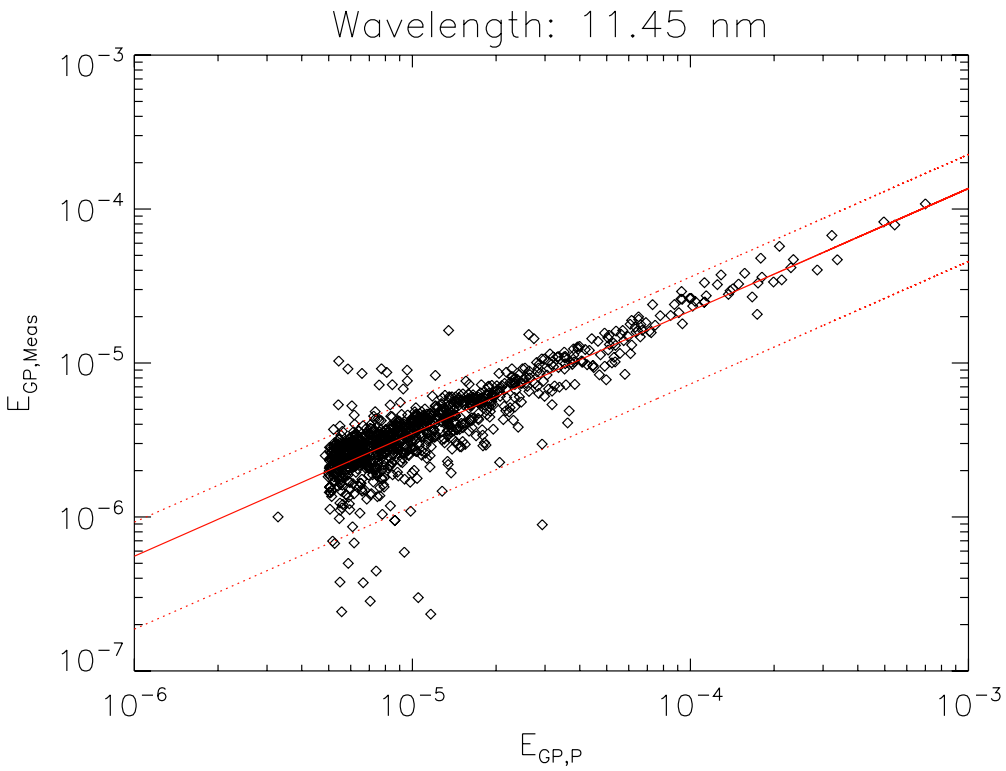

Figure 9. FISM2 flare fit (solid red) and $\pm 1\sigma$ error (dashed red) for the gradual phase component in the 11.45 nm bin that contains the hot Fe XXII emission line at 11.44 nm. This is the fit and error for the $E_{GP,P}$ proxy from GOES XRS-B and the SDO/EVE $E_{GP,Meas}$ 11.45 nm 0.1 nm co-temporal measurement bin points in black

in black. This plot is shown with log/log X/Y axes, so the expected power law fit shows up as a linear relationship, as shown and explained with Eq. 14. This wavelength bin is dominated by the hot Fe XXII emission line formed at $log(T) = 7.1$. The derived $\pm 1\sigma$ errors are shown as the dashed red lines, showing a constant percent error.

Once these relative uncertainties are found for each component, the daily, impulsive phase, and gradual phase, at the given time, t, then these absolute uncertainties are the root-sum-squared (RSS) to determine the final absolute uncertainty at the modeled time.

$$\sigma_{Flare}(\lambda, t) = \sqrt{\sigma_{Daily}(\lambda, d)^2 + \sigma_{IP,Flare}(\lambda, t)^2 + \sigma_{GP,Flare}(\lambda, t)^2} \tag{22}$$

If there are no impulsive and/or gradual phase contributions at a given time, then the RSS will not have additional uncertainty contributions from these components and both the irradiance and the uncertainty at that time, t, will be the same as the respective daily values on for the day, d. In the final FISM2 data product the uncertainty presented is the relative uncertainty, so it is this absolute uncertainty, $\sigma_{Flare}(\lambda, t)$, divided by the FISM2 irradiance prediction at that time. The percent uncertainty can then be found simply by multiplying this relative uncertainty given in the data product by 100.

4 FISM2 Results

All empirical model coefficients have been found using relations and algorithms discussed in the previous section. With these now fit and coefficients found, anytime the proxy is available a FISM2 solar irradiance estimate can be produced. Combining the solar minimum, solar cycle, solar rotation gives a FISM2 daily estimate every day as far back as 1947 when F10.7 daily proxy is available, while adding the two flare components due to the gradual and impulsive phases when the GOES XRS is available to this daily estimate gives the final FISM2 solar flare irradiance estimate every 60 s as far back as 1981.

4.1 FISM2 Solar Minimum Spectrum Results

The FISM2 solar minimum reference spectrum is given in Fig. 10. This FISM2 reference spectrum is also compared to the Whole Heliosphere Interval (WHI) solar minimum reference spectrum (Woods et al., 2009; Chamberlin, Woods, Crotser, et al., 2009) in orange, and also to the NRLEUV-2 minimum spectrum (Warren, 2005), seen in green, at wavelengths where it is available below 120 nm. Given that the SORCE/XPS Level 4 data goes from 0.1-40 nm, as seen in blue, FISM2 models this entire range, but only uses these results in the final merged product from 0.1-6.0 nm when the SDO/EVE model results, shown in red, are used in favor as they are more accurate actual measurements. The FISM2 solar minimum spectrum based on SORCE/SOLSTICE is shown in black.

Results throughout the XUV and EUV wavelengths at low irradiance values in-between the stronger emission lines and absent of strong underlying continua show much higher values than the NRLEUV-2 reference spectrum. The NRLEUV-2 reference spectrum was created from the CHIANTI model, and therefore can achieve much higher spectral resolution and lower signal level calculations than can be realistically measured. This is evident in comparisons at the low irradiance levels of EVE, and similarly modeled by FISM2, in the low-irradiance levels below around 10^{-6} $W/m^2/nm$ levels mainly between emission lines that are around 1-2 data numbers (DN) as shown by Hock et al. (2012) that are measurement noise floor in EVE.

The WHI spectrum was compiled from an opportunistic EVE sounding rocket flight (6.0-105.0 nm) that occurred on 14 April 2008 prior to the SDO/EVE launch, as well as the average TIMED/SEE (105.0-116.0 nm) and SORCE/XPS (0-6.0 nm) and SOLSTICE (116-310 nm) measurements from 10-16 April 2008 to fill in wavelengths not covered by SDO/EVE. Although close, these measurements were not exactly at solar minimum and occurred at an average F10.7 of 68.9 and sunspot number of 2.0

4.2 FISM2 Daily Model Results

With FISM2 proxies going back until 1947 with F10.7, albeit with more representative ones continuing to become routinely measured, FISM2 is able to make a daily average spectrum for every day since then. Fig. 11 shows the integrated 0-105 nm wavelength range estimations over these six-and-a-half solar cycles starting at the peak of solar cycle 18 in 1947 and continually updating as we presently head into the start of solar cycle 25. This figure shows the difference in solar irradiance output from one solar cycle to another, as well as the decrease in the solar cycle maximum over the past three cycles. These long-term FISM2 results accurately quantifying the differing amount of long-term solar ultraviolet energy into the planetary systems may be used for potential climate studies.

FISM2 can be compared to the base measurement data sets for which they were derived over the time the measurements were available to quantify the uncertainties in the FISM2 estimates. This can be done for every one of the 1900 FISM2 wavelength bins, but only a select few are shown here in each range. An example XUV emission is shown

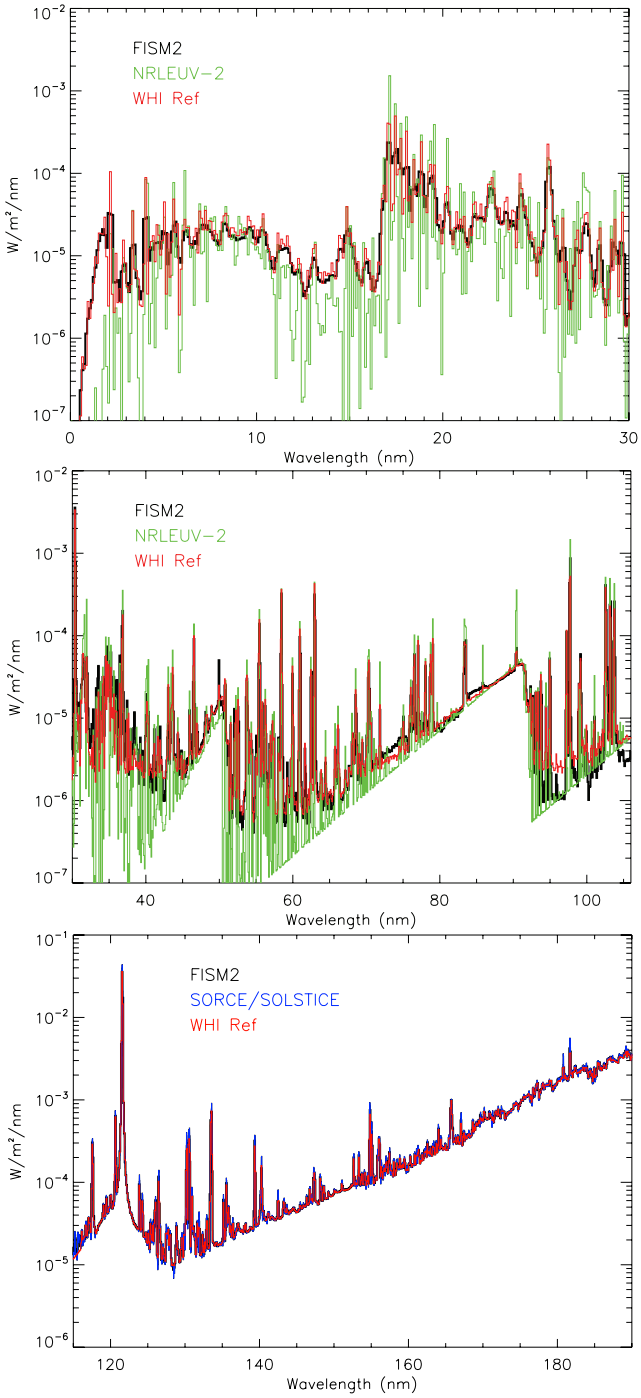

Figure 10. The FISM2 solar minimum reference spectrum compared to those from WHI (red) and NRLEUV-2 (green) as well as SORCE/SOLSTICE. The top panel is for wavelengths from 0-30 nm, the middle panel from 30-105 nm, and the bottom from 115-190nm.

584 at the top of Fig. 12 for the 1.05 nm bin (1.00-1.10 nm), which is dominated by the Bremsstrahlung
585 continuum. Shown are the SORCE/XPS Level 4 model product over the range of the

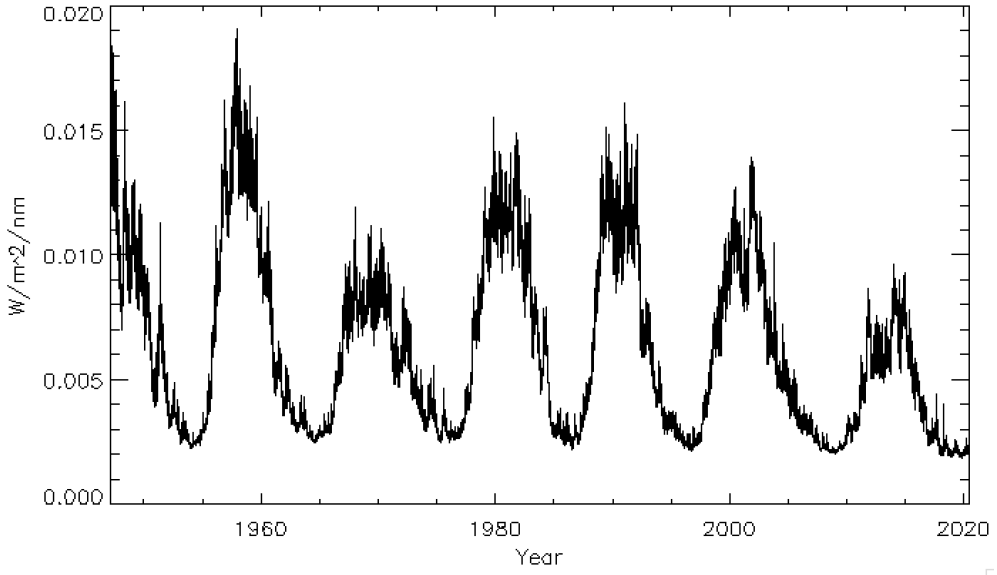

Figure 11. FISM2 daily results integrated over 0-105 nm from 1947 to June 2020.

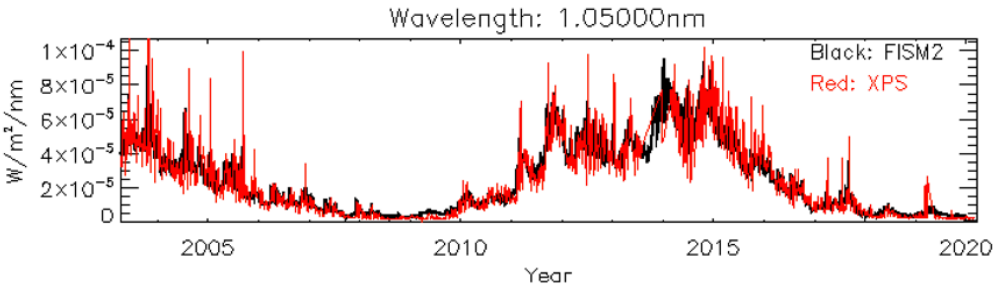

Figure 12. FISM2 results for the 1.05 nm bin (black) compared to the SORCE/XPS/L4 product (red) on the top.

SORCE mission as well as the FISM2 'daily' estimates for this bin. The uncertainties at this wavelength bin are constant over this time period at approximately 12% as they are all modeled using the F10.7 proxy.

For example FISM2 results in the EUV range, the 30.35 nm bin containing the strong He II 30.34 nm emission line is shown on the bottom in Fig. 13 and the hot 9.39 nm emission line containing the Fe XVIII emission line is presented on the top. The black line is the FISM2, the red line is the EVE V6 data product, which FISM2 is based on, while the EVE V7 is the upcoming data product. This give two examples of a strong optically thick emission formed in the chromosphere as well as a hot coronal emission that is only found in hot active regions and flares. These are EVE measurements from the MEGS-A channel, which failed in May 2014. When the He II 30.34 nm emission line is available from MEGS-A channel of EVE to use as a proxy, then the model is very accurate with an uncertainty of only about 0.8%, as it should be if the proxy and base measurement are the same measurement, but if a backup proxy is needed before and after the MEGS-A failure, the uncertainty of the FISM2 model goes up to around 2.2%.

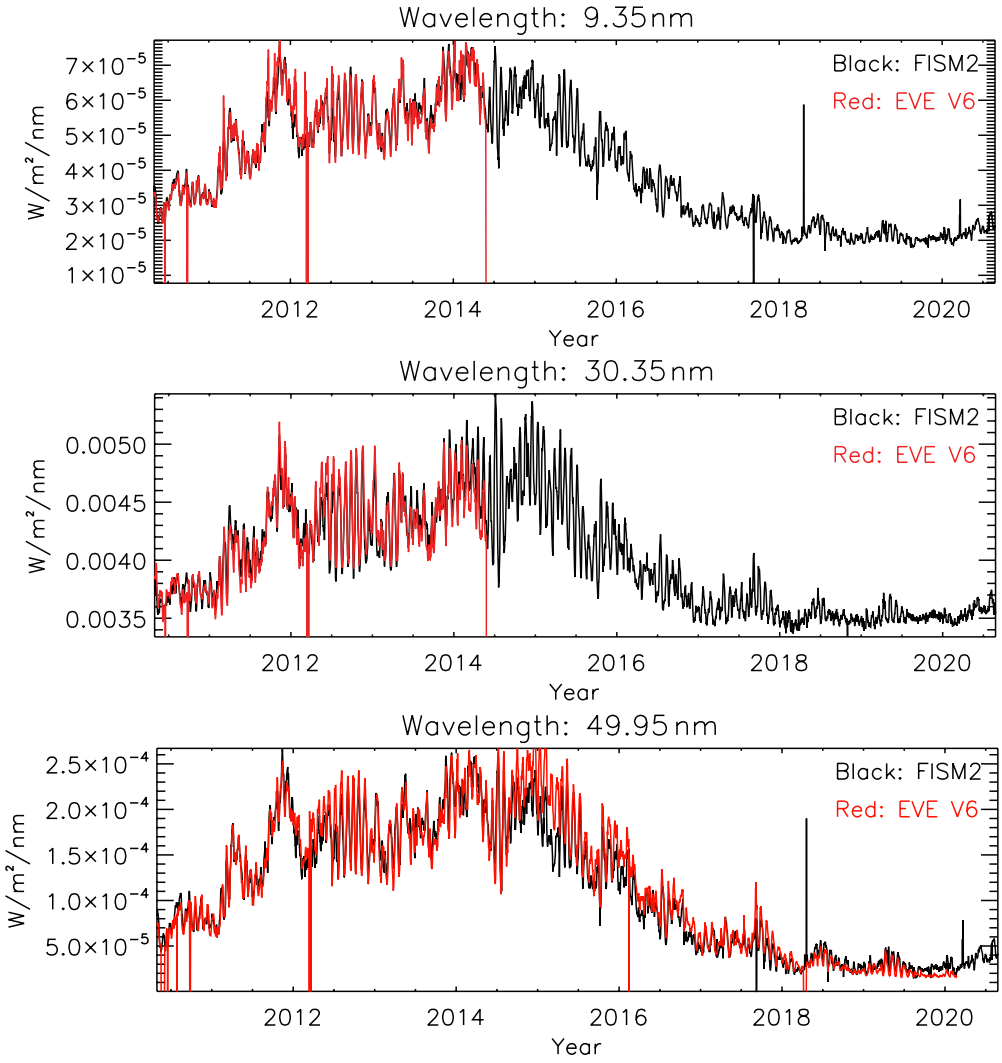

Figure 13. FISM2 daily results (black) for the 9.35 nm bin (top), 30.35 nm bin (middle), and 49.95 nm bin (bottom) compared to the SDO/EVE V6 (red) data. The EVE MEGS-A wavelengths (6-33nm) end in May 2014 when that channel failed, while the MEGS-B wavelengths (33-105nm) continue.

Finally, for an example in the FUV, the strong H I Lyα line (121.56 nm, left) in the 121.55 nm FISM2 bin as well as the hot Fe XXI (135.41 nm, right) emission line in the 135.45 nm bin are shown in Fig. 14 for both the SORCE/SOLSTICE (red) measurements and the FISM2 estimates (black). The SORCE/SOLSTICE data are only shown until 2017 as FISM2 is trained to the SOLSTICE V15 data product, where the current version is V17. The full cadence, native resolution product that is used for the 'flare' product is only currently available up to V15, so to stay consistent between the daily and flare FISM2 products and training the most recently available consistent level product was used, which is V15, which has not been processed for data at this version after 2017. The percent uncertainty is relatively smaller in the FUV bins than in the EUV and XUV, as will be shown later in Fig. 15, but the absolute magnitude of the variability over the

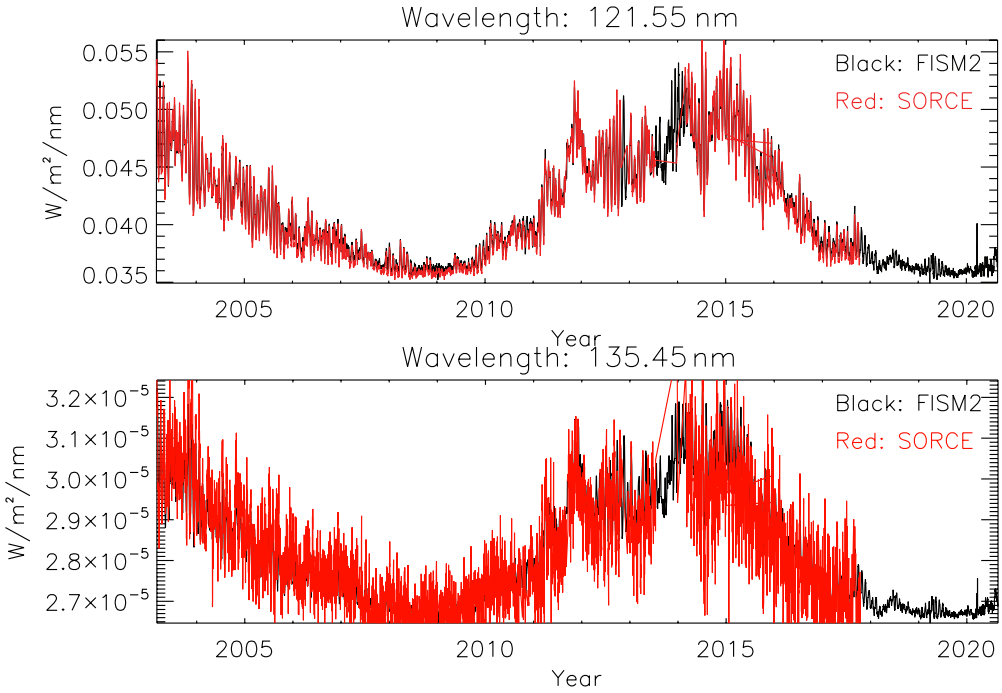

Figure 14. FISM2 daily results (black) for the 121.55 nm bin (top) and 135.45 nm bin (bottom) compared to the SORCE/SOLSTICE V15 data (red).

solar cycle and solar rotations in the FUV are also smaller, as is also shown later in Fig. 19.

It is clear in Figs. 12, 13, and 14 that the solar cycle variations and magnitudes agree very well with the measured solar cycle at all phases of the solar cycle, even at solar cycle minimum times when some proxies, e.g. F10.7, tend to bottom out relative to other proxies and measurements. Also looking at the higher-frequency solar rotation timings and magnitudes are modeled well at all wavelengths. This has to do with the numerous proxies used representing the different temperatures of the solar atmosphere, and therefore can account for the center-to-limb variations and optical thickness effects of active regions as they move from the limb across the face of the Sun, as was described in more detail by Worden et al. (2001) and Chamberlin et al. (2007).

The daily uncertainties for each wavelength depend on what proxies are available that day, so can change if the optimal proxy is not available. The spectrum of uncertainties for a recent day, here 1 January 2020, where all the optimal proxies for each wavelength are available and used, are are shown on the bottom in Fig. 15 along with the FISM2 solar spectrum for that day on the top. The FISM2 errors range from around 2% up to 200%, and are highly correlated with the accuracies of the measurements FISM2 is based on. Where the simple interpolation is used to fill the gap between 105 and 115 nm, there are large uncertainties set at >1000% as these results are not based on any actual measurements.

The largest errors occur where the measurements are not that good. One example is in between the strong emission lines in the SDO/EVE measurements the signal-to-noise ratio (SNR) is not that good, and therefore the solar variations are not measured as accurately, and therefore cannot be modeled as well as the strong emission lines

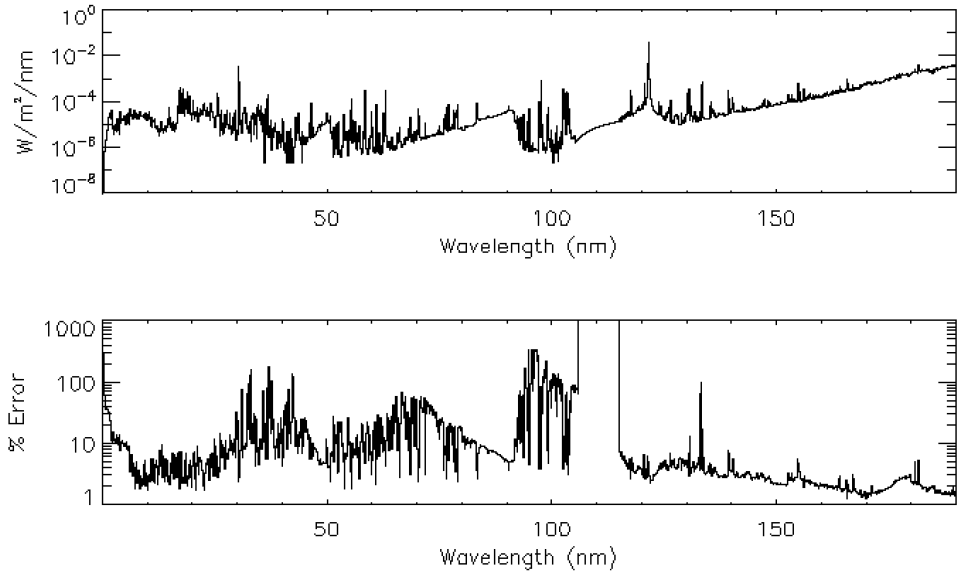

Figure 15. The FISM2 daily spectrum for 1 January 2020 on top, along with the spectrum of uncertainties for each bin on the bottom.

and continua that have high SNR. The FUV has good low FISM2 errors, as SORCE/SOLSTICE measurements have very good SNR and low uncertainties in its measurements throughout its range. The solar variations themselves also contribute, as the solar cycle and rotational variations themselves are lower in the FUV, only changing by about a factor of two, leading to lower percent errors in the modeling of these variations. That is in contrast to the short XUV wavelengths that have solar cycle variations that can change by over an order of magnitude, so these large variations are well modeled only between 10% and 100% error.

4.3 FISM2 Solar Flare Results

FISM2 comparisons to the base data sets at higher cadence also show good agreement within the stated uncertainties for solar flare variations. A small subset of the comparisons that can be made are presented here to show the agreement of FISM2 estimations to the measurements for which the empirical model was trained.

Starting with the XUV, time series for the 0.1 nm wavelength bin centered at 1.95 nm (e.g. 1.90 to 1.99 nm) for both the FISM2 estimation, in red, as well as the SORCE/XPS L4 data, in black, are given for the large X17 class flare on 28 Oct 2003 in Fig. 16. This wavelength bin is near the peak of the hot free-free Bremsstrahlung continuum that is significantly enhanced during the thermal phase of solar flares. This shows very good agreement between the FISM2 model and the XPS base data set, with both of the irradiance increasing by over an order of magnitude. The uncertainties shown are around 15% for the daily model, and go up to around 23% with the additional gradual flare component (remember there is not impulsive phase contributions for wavelength below 6 nm). In fact, early on and then again late in the flare, there is actually an improvement in the accuracy of the FISM2 flare product that is better than the daily model. This is attributed to the lower absolute standard deviations in the high-cadence fits between the GOES XRS proxy and the SORCE/XPS data, which are slightly better at some magnitudes than the daily fit.

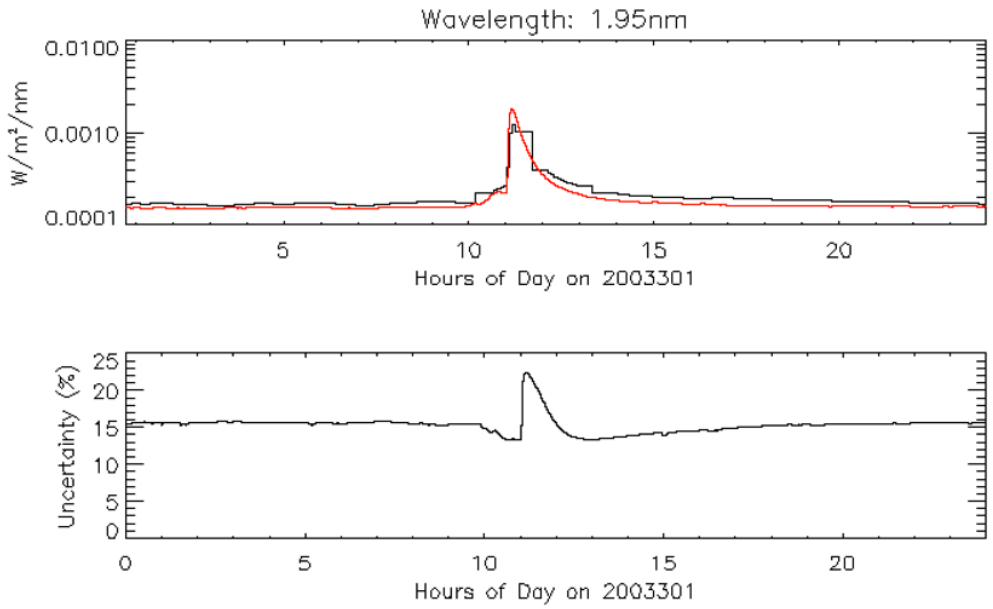

Figure 16. FISM2 (red) and SORCE/XPS (black) Level 4 model results for the 1.95 nm wavelength bin on the top, while the FISM2 time-dependent uncertainties for this wavelength bin and times are shown on the bottom.

The top panels of Fig. 17 shows the FISM2 'flare' results compared to the SDO/EVE measurements of this bin, while the bottom panels of Fig. 17 shows the uncertainties at every time. This is for one hour of time on 9 March 2011, early in the SDO mission when an X1.1 flare occurred near the center of the solar disk (N08, W09) and during the time the EVE/MEGS-A channel was still operational for comparison. The flare time series shows the total FISM2 flare estimation (black) for this 0.1 nm bin compared to the 0.1 nm bin SDO/EVE times series (red). Also shown are the individual FISM2 model components, which summed together equal the total FISM2 flare. These are the daily average component (light blue), which consists of the sum of the solar cycle and solar rotation components, and the impulsive phase (green) and gradual phase (purple) flare components. The EVE data are at 10 s cadence while the FISM2 is at 60 s cadence. The uncertainty, as discussed in a later section in further detail, is calculated as an absolute value using the fit of the EVE data to the proxies, and therefore when using this absolute value to calculate a percent uncertainty, the percent is inversely proportional to the magnitude of the irradiance.

The left panels in Fig. 17 are for the 30.35 nm bin showed in many previous results. This strong He II 30.38 nm chromospheric emission line has a strong impulsive phase component early in the flare. The right panels in Fig. 17 shows another FISM2 (red) and SDO/EVE (black) time series during the same flare, but this time for the 0.1 nm bins centered at 10.05 nm containing the Fe XVII 10.08 nm emission line formed at $log(T) = 7.2$. The magnitude of the emission is accurately represented by FISM2, but the timing will always be at the GOES XRS timing that is its proxy. This timing discrepancy is known and shown in the EVE data as the hot flaring plasma cools from $> 10MK$ down through the contributions functions of the various emission lines (Ryan et al., 2013). This timing shift, as well as the time series broadening, is not yet corrected for in FISM2 but is planned for future FISM released based on empirical corrections found in the Enthalpy Based Thermal Element Model (EBTEL) (Thiemann, Eparvier, & Woods, 2017). In com-

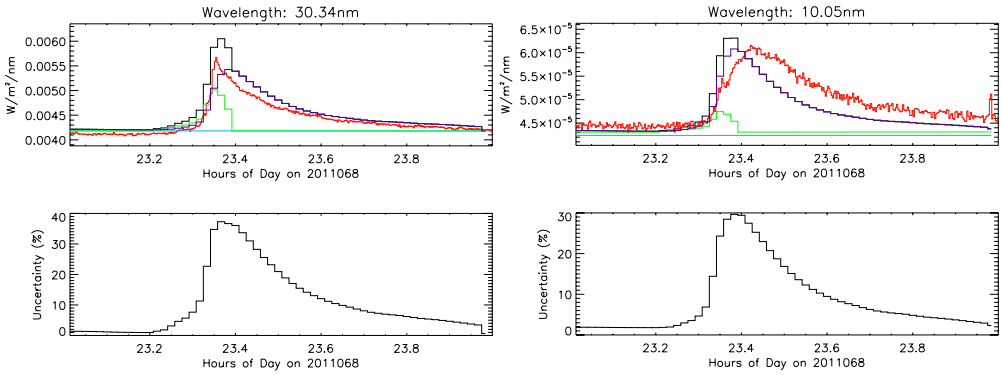

Figure 17. FISM2 results for a strong flare that occurred on 9 March 2011 that was also observed by SDO/EVE in the 30.35 nm (left) and 10.05 nm (right) wavelength bins. Not only shown is the total FISM 'flare' model results (black) compared to the SDO/EVE measurements (red) for the two wavelength bins, but also the individual components that make up the FISM2 'flare' model: the FISM2 'daily' values (light blue) along with the impulsive phase (green) and gradual phase (purple) components.

parison of the flare components, it is easily seen that the cool chromospheric He II flare emissions are dominated by the impulsive phase early in the flare, while the hot Fe XIX flare line is dominated by the gradual phase thermal emissions.

Comparisons of the FISM2 flare results to SOLSTICE have also been made during the validation process, and one example is shown here in Fig. 18. Remembering that SOLSTICE is a spectrometer that only measures a single wavelength at a given time and must scan the grating over the wavelength range to compile a complete spectrum, comparisons at any given time can be complicated. Fortunately, SORCE operations does routine, high cadence scans across the strong H I Lyα emission line at 121.57 nm that is within the 121.55 nm FISM2 bin, its broad wings, and also the Si III emission line at 120.65 nm. This scan goes from 120.5 nm to around 122.75 nm.

SOLSTICE was fortunately doing one of the aforementioned Lyα scans near the peak of the large X17 solar flare on 28 October 2003. Fig. 18 compares these SOLSTICE results to the FISM2 results, where the FISM2 results were at the peak of the flare and the SOLSTICE measurements were mostly within 10 minutes of the flare peak. The SOLSTICE results are put into 0.03 nm bins based on the recorded central wavelength in the high spectral-resolution data set, while FISM2 results are in their standard 0.1 nm bins. Noticeable dips are seen in the SOLSTICE flare spectra and ratio, where these 0.3 nm bins did not record a measurement within them during the flare peak scan (>60 minutes from the peak) so are at or near the daily values. There is very good agreement for this flare, where both the SOLSTICE and FISM2 estimates show broad enhancements in the Lyα wings. These increases are a small percent, but still large absolute, increases for the flare that are consistent with FISM1 estimations of this line. There is also a large percent increase seen in the Si III emission line.

4.4 FISM2 Solar Variation Comparison

With FISM2 able to accurately model all timescales of solar variations across the full range of wavelengths from 0-190 nm, interesting and comprehensive comparisons of these wavelength can be performed that limited measurements can not. Figs. 19 and 20 show all four modeled solar variations across the entire modeled wavelength range. The

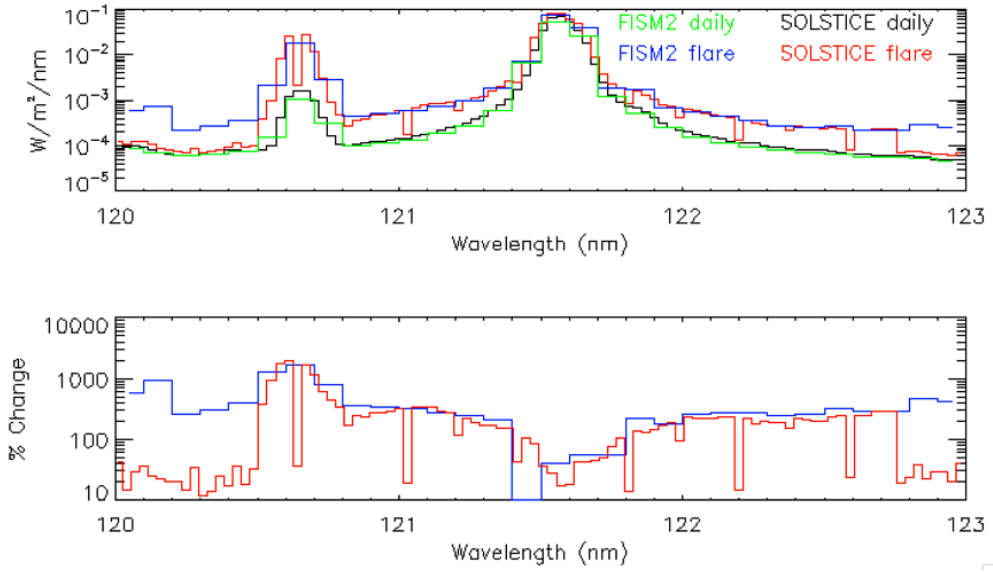

Figure 18. FISM2 'daily' (green) and 'flare' (blue) results for the solar flare that occurred on 28 Oct 2003 compared to the SORCE/SOLSTICE daily (black) and flare (red) measurements that occurred at various times but near the peak at the top. The FISM2 'flare' spectrum is at the peak of the GOES XRS-B channel. The bottom also shows the percent change in the flare irradiance spectra over their daily values.

absolute modeled spectra are given in the top, while the bottom plot of Fig. 19 shows the percent change for the respective solar variations.

The solar cycle and solar rotational variations show that the shorter, higher energy wavelengths formed at hotter temperatures have a much larger percent variability than the cooler emissions, as expected. The solar cycle variability is also approximately 10x larger than the solar rotation variations across all wavelengths.

There are many strong emission lines formed in the chromosphere and transition region that show very strong impulsive phase enhancements, as expected (Chamberlin et al., 2008; Woods et al., 2011), while hot, thermal plasma in the XUV wavelengths also shows the desired strong gradual phase increases by orders of magnitude. There were many wavelength bins that did not exhibit a strong flare signal, especially in the limited data from the MEGS-B region (33-105nm), and many times cause erroneously large flare signals with the associated extremely large standard deviations; the flare fits with large standard deviations were eliminated in the respective wavelength bins so as not to have a flare contribution. These show up as the gaps in the lower plot of Fig. 20.

4.5 FISM2 Data Access

FISM2 data products are available through the LASP Solar Irradiance Data Center (LISIRD) `https://lasp.colorado.edu/lisird/` in both the 'daily' and 'flare' products. Through the LISIRD site, both time and spectral ranges of interest can be set to provide quick plotting and then downloading in user-specified formats. Also available are each of the products in the wavelength binning scheme described in (Solomon & Qian, 2005) to ease ingestion of FISM2 products as a driver for TIME-GCM, WACCM/WACCM-X, or other Ionosphere-Thermosphere-Mesosphere (ITM) models that are driving by this

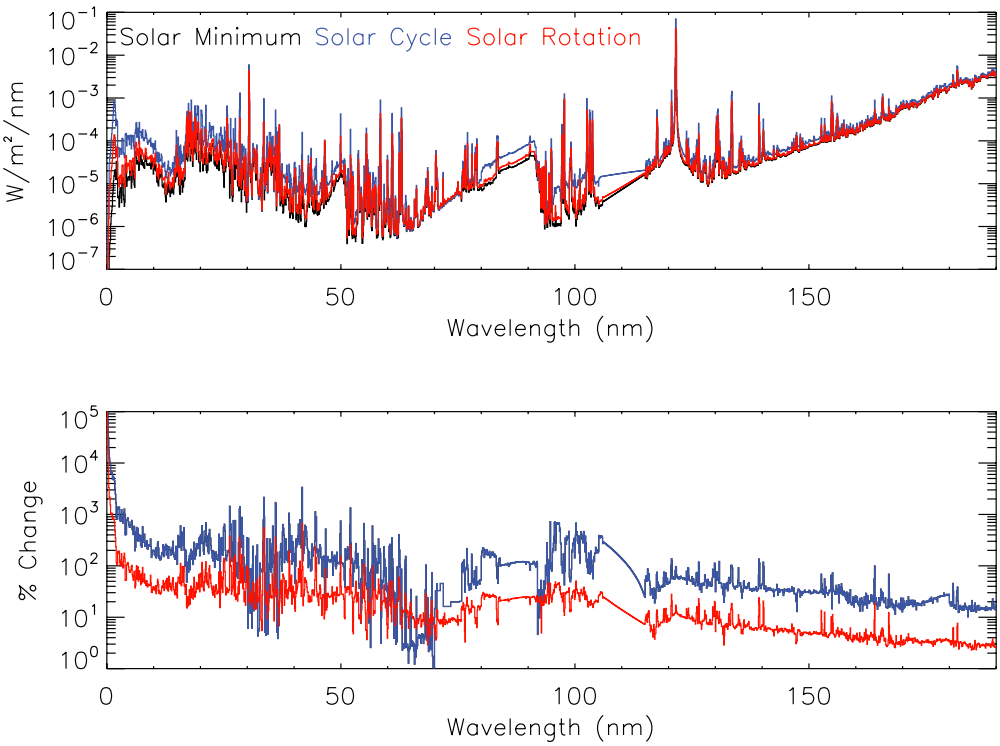

Figure 19. FISM2 absolute irradiance changes (top) and percent changes (bottom) across the entire FISM2 modeled wavelength range for solar cycle (blue) and solar rotation (red) variations. The solar cycle and the solar rotation variations shown are the 90th percentile of the respective maximum solar variations that have occurred from 1947-present.

common scheme. Each of the FISM2 products are also available for direct download of the files at `http://lasp.colorado.edu/eve/data_access/evewebdata/fism/` to ease scripts and other data access protocols that can bypass the LISIRD interface, if desired.

There is a FISM2 ReadMe file located at `http://lasp.colorado.edu/eve/data_access/eve_data/fism/FISM2_ReadMe.pdf`, which explains the data arrays found in the files and their units to ease use of FISM2.

5 Conclusion

FISM2 is vastly improved over the original FISM model, being based on more accurate data sets, more flares and longer time series, as well as improving to 0.1 nm bins. This in turn will provide more accurate solar irradiance driver for space weather and climate studies of the Earth and other studies of planetary ionospheres and thermospheres.

The significant advances provided by FISM2 warranted a release of this product, but many improvements are already identified and are planned for implementation in the future. These include 1) using MinXSS as a driver in the 0.1-2.0 nm wavelength range, 2) using GOES-16^{+} data products, specifically the EUVS channels, as proxies to improve the impulsive phase modeling, 3) implementing a temperature dependent EBTEL-like flare peak and time-series broadening of the flare emissions, and 4) continuing to update FISM2 empirical relationships when new versions of base data products become avail-

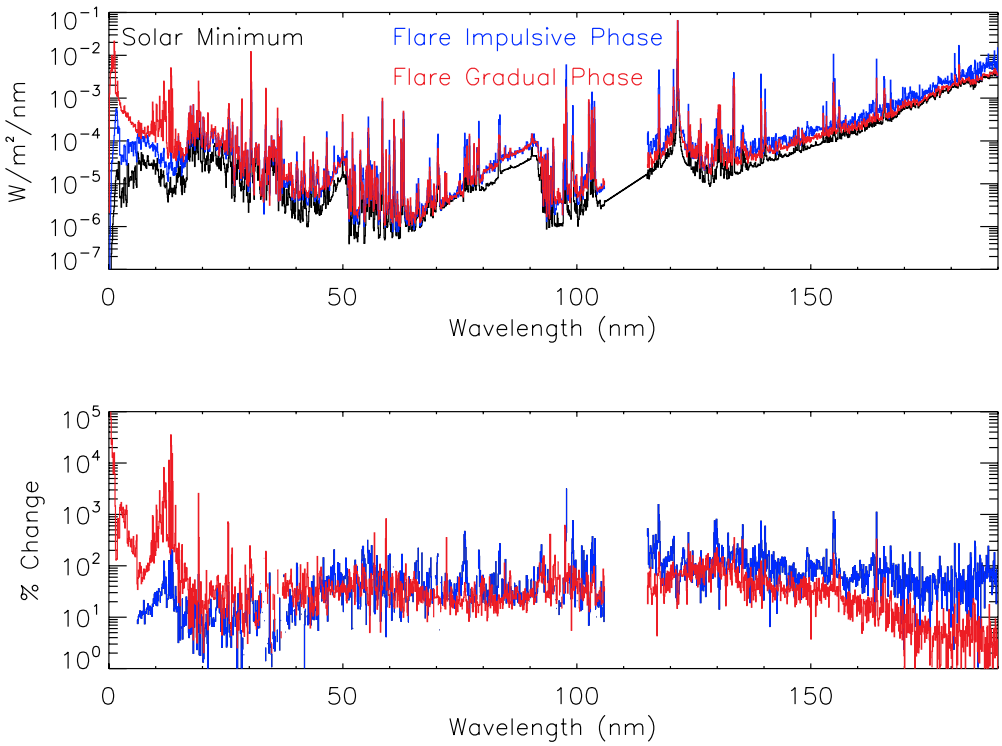

Figure 20. FISM2 absolute irradiance changes (top) and percent changes (bottom) across the entire FISM2 modeled wavelength range for the solar flare impulsive phase (blue) and gradual phase (red) variations. The FISM2 solar minimum reference spectrum is also shown in the top plot in black. The flare changes are during the respective impulsive and gradual phase peaks of the 28 Oct 2003 X17 flare.

able, such as SORCE/SOLSTICE V17 and SDO/EVE V7 that are already released or soon will be.

Acknowledgments

The authors acknowledge NASA support at CU/LASP from NASA contracts NAS5-02140 (SDO), NNH10CC04C (MAVEN), and NAS5-97045 (SORCE) and from NASA grants NNX16AE86G (LWS TR&T) and NNZ17A171G (H-TIDES MinXSS CubeSat).

SORCE/XPS and SORCE/SOLSTICE data are available at `https://lasp.colorado.edu/home/sorce/data/`. SDO/EVE data are available at `https://lasp.colorado.edu/home/eve/data/`. FISM2 data are available at `https://lasp.colorado.edu/lisird/`. GOES XRS data are available at `https://www.ngdc.noaa.gov/stp/satellite/goes/`.

References

Cargill, P. J., Mariska, J. T., & Antiochos, S. K. (1995, February). Cooling of Solar Flare Plasmas. I. Theoretical Considerations. *Astrophys. J.*, *439*, 1034. doi: 10.1086/175240

Caspi, A., & Lin, R. P. (2010, December). RHESSI Line and Continuum Observations of Super-hot Flare Plasma. *Astrophys. J. Letters*, *725*(2), L161-L166. doi: 10

.1088/2041-8205/725/2/L161

Chamberlin, P. C., Woods, T. N., Crotser, D. A., Eparvier, F. G., Hock, R. A., & Woodraska, D. L. (2009, March). Solar cycle minimum measurements of the solar extreme ultraviolet spectral irradiance on 14 April 2008. *Geophys. Res. Lett.*, *36*(5), L05102. doi: 10.1029/2008GL037145

Chamberlin, P. C., Woods, T. N., & Eparvier, F. G. (2007, July). Flare Irradiance Spectral Model (FISM): Daily component algorithms and results. *Space Weather*, *5*(7), S07005. doi: 10.1029/2007SW000316

Chamberlin, P. C., Woods, T. N., & Eparvier, F. G. (2008, May). Flare Irradiance Spectral Model (FISM): Flare component algorithms and results. *Space Weather*, *6*(5), S05001. doi: 10.1029/2007SW000372

Chamberlin, P. C., Woods, T. N., Eparvier, F. G., & Jones, A. R. (2009, August). Next generation x-ray sensor (XRS) for the NOAA GOES-R satellite series. In *Proc. SPIE* (Vol. 7438, p. 743802). doi: 10.1117/12.826807

Dere, K. P., Landi, E., Mason, H. E., Monsignori Fossi, B. C., & Young, P. R. (1997, October). CHIANTI - an atomic database for emission lines. *Astronomy & Astrophysics Supp.*, *125*, 149-173. doi: 10.1051/aas:1997368

Dere, K. P., Landi, E., Young, P. R., Del Zanna, G., Landini, M., & Mason, H. E. (2009, May). CHIANTI - an atomic database for emission lines. IX. Ionization rates, recombination rates, ionization equilibria for the elements hydrogen through zinc and updated atomic data. *Astronomy & Astrophysics*, *498*(3), 915-929. doi: 10.1051/0004-6361/200911712

Didkovsky, L., Judge, D., Wieman, S., Woods, T., & Jones, A. (2012, January). EUV SpectroPhotometer (ESP) in Extreme Ultraviolet Variability Experiment (EVE): Algorithms and Calibrations. *Solar Phys.*, *275*(1-2), 179-205. doi: 10.1007/s11207-009-9485-8

Emslie, A. G., Dennis, B. R., Shih, A. Y., Chamberlin, P. C., Mewaldt, R. A., Moore, C. S., ... Welsch, B. T. (2012, November). Global Energetics of Thirty-eight Large Solar Eruptive Events. *Astrophys. J.*, *759*(1), 71. doi: 10.1088/0004-637X/759/1/71

Eparvier, F. G., Chamberlin, P. C., Woods, T. N., & Thiemann, E. M. B. (2015, December). The Solar Extreme Ultraviolet Monitor for MAVEN. *Sp. Sci. Rev.*, *195*(1-4), 293-301. doi: 10.1007/s11214-015-0195-2

Garcia, H. A. (1994, October). Temperature and Emission Measure from Goes Soft X-Ray Measurements. *Solar Phys.*, *154*(2), 275-308. doi: 10.1007/BF00681100

Harada, Y., Poppe, A. R., Halekas, J. S., Chamberlin, P. C., & McFadden, J. P. (2017, June). Photoemission and electrostatic potentials on the dayside lunar surface in the terrestrial magnetotail lobes. *Geophys. Res. Lett.*, *44*(11), 5276-5282. doi: 10.1002/2017GL073419

Hock, R. A., Chamberlin, P. C., Woods, T. N., Crotser, D., Eparvier, F. G., Woodraska, D. L., & Woods, E. C. (2012, January). Extreme Ultraviolet Variability Experiment (EVE) Multiple EUV Grating Spectrographs (MEGS): Radiometric Calibrations and Results. *Solar Phys.*, *275*(1-2), 145-178. doi: 10.1007/s11207-010-9520-9

Hurrell, J. W., Holland, M. M., Gent, P. R., Ghan, S., Kay, J. E., Kushner, P. J., ... Marshall, S. (2013, September). The Community Earth System Model: A Framework for Collaborative Research. *Bulletin of the American Meteorological Society*, *94*(9), 1339-1360. doi: 10.1175/BAMS-D-12-00121.1

Jakosky, B. M., Lin, R. P., Grebowsky, J. M., Luhmann, J. G., Mitchell, D. F., Beutelschies, G., ... Zurek, R. (2015, December). The Mars Atmosphere and Volatile Evolution (MAVEN) Mission. *Sp. Sci. Rev.*, *195*(1-4), 3-48. doi: 10.1007/s11214-015-0139-x

Lollo, A., Withers, P., Fallows, K., Girazian, Z., Matta, M., & Chamberlin, P. C. (2012, May). Numerical simulations of the ionosphere of Mars during a solar

flare. *Journal of Geophysical Research (Space Physics)*, *117*(A5), A05314. doi: 10.1029/2011JA017399

Marsh, D. R., Mills, M. J., Kinnison, D. E., Lamarque, J.-F., Calvo, N., & Polvani, L. M. (2013, October). Climate Change from 1850 to 2005 Simulated in CESM1(WACCM). *Journal of Climate*, *26*(19), 7372-7391. doi: 10.1175/JCLI-D-12-00558.1

Mason, J. P., Woods, T. N., Caspi, A., Chamberlin, P. C., Moore, C., Jones, A., ... Solomon, S. C. (2016, March). Miniature X-Ray Solar Spectrometer: A Science-Oriented, University 3U CubeSat. *Journal of Spacecraft and Rockets*, *53*(2), 328-339. doi: 10.2514/1.A33351

Mason, J. P., Woods, T. N., Chamberlin, P. C., Jones, A., Kohnert, R., Schwab, B., ... Warren, H. (2020, July). MinXSS-2 CubeSat mission overview: Improvements from the successful MinXSS-1 mission. *Advances in Space Research*, *66*(1), 3-9. doi: 10.1016/j.asr.2019.02.011

McClintock, W. E., Rottman, G. J., & Woods, T. N. (2005, August). Solar-Stellar Irradiance Comparison Experiment II (Solstice II): Instrument Concept and Design. *Solar Phys.*, *230*(1-2), 225-258. doi: 10.1007/s11207-005-7432-x

Milligan, R. O., Hudson, H. S., Chamberlin, P. C., Hannah, I. G., & Hayes, L. A. (2019, October). Lyman-alpha Variability During Solar Flares Over Solar Cycle 24 Using GOES-15/EUVS-E. *arXiv e-prints*, arXiv:1910.01364.

Moore, C. S., Chamberlin, P. C., & Hock, R. (2014, May). Measurements and Modeling of Total Solar Irradiance in X-class Solar Flares. *Astrophys. J.*, *787*(1), 32. doi: 10.1088/0004-637X/787/1/32

Neupert, W. M. (1968, July). Comparison of Solar X-Ray Line Emission with Microwave Emission during Flares. *Astrophys. J. Letters*, *153*, L59. doi: 10.1086/180220

Neupert, W. M. (1989, September). Transient Coronal Extreme Ultraviolet Emission before and during the Impulsive Phase of a Solar Flare. *Astrophys. J.*, *344*, 504. doi: 10.1086/167819

Pesnell, W. D., Thompson, B. J., & Chamberlin, P. C. (2012, January). The Solar Dynamics Observatory (SDO). *Solar Phys.*, *275*(1-2), 3-15. doi: 10.1007/s11207-011-9841-3

Peterson, W. K., Brain, D. A., Mitchell, D. L., Bailey, S. M., & Chamberlin, P. C. (2013, November). Correlations between variations in solar EUV and soft X-ray irradiance and photoelectron energy spectra observed on Mars and Earth. *Journal of Geophysical Research (Space Physics)*, *118*(11), 7338-7347. doi: 10.1002/2013JA019251

Peterson, W. K., Stavros, E. N., Richards, P. G., Chamberlin, P. C., Woods, T. N., Bailey, S. M., & Solomon, S. C. (2009, October). Photoelectrons as a tool to evaluate spectral variations in solar EUV irradiance over solar cycle timescales. *Journal of Geophysical Research (Space Physics)*, *114*(A10), A10304. doi: 10.1029/2009JA014362

Peterson, W. K., Woods, T. N., Fontenla, J. M., Richards, P. G., Chamberlin, P. C., Solomon, S. C., ... Warren, H. P. (2012, May). Solar EUV and XUV energy input to thermosphere on solar rotation time scales derived from photoelectron observations. *Journal of Geophysical Research (Space Physics)*, *117*(A5), A05320. doi: 10.1029/2011JA017382

Qian, L., Burns, A. G., Chamberlin, P. C., & Solomon, S. C. (2010, September). Flare location on the solar disk: Modeling the thermosphere and ionosphere response. *Journal of Geophysical Research (Space Physics)*, *115*(A9), A09311. doi: 10.1029/2009JA015225

Qian, L., Burns, A. G., Chamberlin, P. C., & Solomon, S. C. (2011, October). Variability of thermosphere and ionosphere responses to solar flares. *Journal of Geophysical Research (Space Physics)*, *116*(A10), A10309. doi:

10.1029/2011JA016777

Qian, L., Burns, A. G., Solomon, S. C., & Chamberlin, P. C. (2012, March). Solar flare impacts on ionospheric electrodyamics. *Geophys. Res. Lett.*, *39*(6), L06101. doi: 10.1029/2012GL051102

Rottman, G. (2005, August). The SORCE Mission. *Solar Phys.*, *230*(1-2), 7-25. doi: 10.1007/s11207-005-8112-6

Rottman, G. J., Woods, T. N., & Sparn, T. P. (1993, June). Solar-Stellar Irradiance Comparison Experiment 1. I - Instrument design and operation. *J. Geophys. Res.*, *98*(D6), 10,667-10,677. doi: 10.1029/93JD00462

Ryan, D. F., Chamberlin, P. C., Milligan, R. O., & Gallagher, P. T. (2013, November). Decay-phase Cooling and Inferred Heating of M- and X-class Solar Flares. *Astrophys. J.*, *778*(1), 68. doi: 10.1088/0004-637X/778/1/68

Snow, M., McClintock, W. E., Woods, T. N., White, O. R., Harder, J. W., & Rottman, G. (2005, August). The Mg II Index from SORCE. *Solar Phys.*, *230*(1-2), 325-344. doi: 10.1007/s11207-005-6879-0

Solomon, S. C., & Qian, L. (2005, October). Solar extreme-ultraviolet irradiance for general circulation models. *Journal of Geophysical Research (Space Physics)*, *110*(A10), A10306. doi: 10.1029/2005JA011160

Sternovsky, Z., Chamberlin, P., Horanyi, M., Robertson, S., & Wang, X. (2008, October). Variability of the lunar photoelectron sheath and dust mobility due to solar activity. *Journal of Geophysical Research (Space Physics)*, *113*(A10), A10104. doi: 10.1029/2008JA013487

Thiemann, E. M. B., Chamberlin, P. C., Eparvier, F. G., & Epp, L. (2018, February). Center-to-Limb Variability of Hot Coronal EUV Emissions During Solar Flares. *Solar Phys.*, *293*(2), 19. doi: 10.1007/s11207-018-1244-2

Thiemann, E. M. B., Chamberlin, P. C., Eparvier, F. G., Templeman, B., Woods, T. N., Bougher, S. W., & Jakosky, B. M. (2017, March). The MAVEN EUVM model of solar spectral irradiance variability at Mars: Algorithms and results. *Journal of Geophysical Research (Space Physics)*, *122*(3), 2748-2767. doi: 10.1002/2016JA023512

Thiemann, E. M. B., Eparvier, F. G., & Woods, T. N. (2017, December). A time dependent relation between EUV solar flare light-curves from lines with differing formation temperatures. *Journal of Space Weather and Space Climate*, *7*, A36. doi: 10.1051/swsc/2017037

Warren, H. P. (2005, March). A Solar Minimum Irradiance Spectrum for Wavelengths below 1200 Å. *Astrophys. Journal Supp.*, *157*(1), 147-173. doi: 10.1086/427171

Woods, T. N., Chamberlin, P. C., Harder, J. W., Hock, R. A., Snow, M., Eparvier, F. G., ... Richard, E. C. (2009, January). Solar Irradiance Reference Spectra (SIRS) for the 2008 Whole Heliosphere Interval (WHI). *Geophys. Res. Lett.*, *36*(1), L01101. doi: 10.1029/2008GL036373

Woods, T. N., Chamberlin, P. C., Peterson, W. K., Meier, R. R., Richards, P. G., Strickland, D. J., ... Tsurutani, B. T. (2008, August). XUV Photometer System (XPS): Improved Solar Irradiance Algorithm Using CHIANTI Spectral Models. *Solar Phys.*, *250*(2), 235-267. doi: 10.1007/s11207-008-9196-6

Woods, T. N., Eparvier, F. G., Bailey, S. M., Chamberlin, P. C., Lean, J., Rottman, G. J., ... Woodraska, D. L. (2005, January). Solar EUV Experiment (SEE): Mission overview and first results. *Journal of Geophysical Research (Space Physics)*, *110*(A1), A01312. doi: 10.1029/2004JA010765

Woods, T. N., Eparvier, F. G., Hock, R., Jones, A. R., Woodraska, D., Judge, D., ... Viereck, R. (2012, January). Extreme Ultraviolet Variability Experiment (EVE) on the Solar Dynamics Observatory (SDO): Overview of Science Objectives, Instrument Design, Data Products, and Model Developments. *Solar Phys.*, *275*(1-2), 115-143. doi: 10.1007/s11207-009-9487-6

Woods, T. N., Hock, R., Eparvier, F., Jones, A. R., Chamberlin, P. C., Klimchuk, J. A., ... Tobiska, W. K. (2011, October). New Solar Extreme-ultraviolet Irradiance Observations during Flares. *Astrophys. J.*, *739*(2), 59. doi: 10.1088/0004-637X/739/2/59

Woods, T. N., Rottman, G., & Vest, R. (2005, August). XUV Photometer System (XPS): Overview and Calibrations. *Solar Phys.*, *230*(1-2), 345-374. doi: 10.1007/s11207-005-4119-2

Woods, T. N., Tobiska, W. K., Rottman, G. J., & Worden, J. R. (2000, December). Improved solar Lyman α irradiance modeling from 1947 through 1999 based on UARS observations. *J. Geophys. Res.*, *105*(A12), 27195-27216. doi: 10.1029/2000JA000051

Worden, J. R., Woods, T. N., & Bowman, K. W. (2001, October). Far-Ultraviolet Intensities and Center-to-Limb Variations of Active Regions and Quiet Sun Using UARS SOLSTICE Irradiance Measurements and Ground-based Spectroheliograms. *Astrophys. J.*, *560*(2), 1020-1034. doi: 10.1086/323058

Xu, S., Liemohn, M. W., Peterson, W. K., Fontenla, J., & Chamberlin, P. (2015, December). Comparison of different solar irradiance models for the superthermal electron transport model for Mars. *Plan. Sp. Sci.*, *119*, 62-68. doi: 10.1016/j.pss.2015.09.008